HHS Public Access

Author manuscript

Mater Sci Eng C Mater Biol Appl. Author manuscript; available in PMC 2021 December 01.

Published in final edited form as:

Mater Sci Eng C Mater Biol Appl. 2020 December ; 117: 111257. doi:10.1016/j.msec.2020.111257.

Empirical and Theoretical Insights into the Structural Effects of Selenite Doping in Hydroxyapatite and the Ensuing Inhibition of Osteoclasts

Victoria M. Wu[1], **M. K. Ahmed**[2], **Mervat S. Mostafa**[3], **Vuk Uskoković**[4]

[1]MP Biomedicals, 9 Goddard, Irvine, CA 92618, USA

[2]Department of Physics, Faculty of Science, Suez University, Suez, Egypt

[3]Science and Technology Center of Excellence (STCE), Ministry of Military Production, Cairo, Egypt

[4]Department of Mechanical and Aerospace Engineering, University of California, Irvine, Engineering Gateway 4200, Irvine, CA 92697, USA

Abstract

The use of ions as therapeutic agents has the potential to minimize the use of small-molecule drugs and biologics for the same purpose, thus providing a potentially more economic and less adverse means of treating, ameliorating or preventing a number of diseases. Hydroxyapatite (HAp) is a solid compound capable of accommodating foreign ions with a broad range of sizes and charges and its properties can dramatically change with the incorporation of these ionic additives. While most ionic substitutes in HAp have been monatomic cations, their lesser atomic weight, higher diffusivity, chaotropy and a lesser residence time on surfaces makes them theoretically bear lessmakes them prone to exert a lesser influence on the material/cell interaction than the more kosmotropic oxyanions. Selenite ion as an anionic substitution in HAp was explored in this study for its ability to affect the short-range and the long-range crystalline symmetry and solubility as well as for its ability to affect the osteoclast activity. We combined microstructural, crystallographic and spectroscopic analyses with quantum mechanical calculations to understand the structural effects of doping HAp with selenite. Integration of selenite ions into the crystal structure of HAp elongated the crystals along the c-axis, but isotropically lowered the crystallinity.

Author CRediT roles: V. M. Wu – Methodology, Supervision, Investigation (biology, Sec.3.3); M. K. Ahmed - Methodology, Formal Analysis, Resources, Visualization, Investigation (ab initio, Sec.3.2), M. S. Mostafa – Methodology, Formal Analysis, Resources, Visualization, Investigation (ab initio, Sec.3.2), V. Uskoković – Conceptualization, Data curation, Methodology, Formal analysis, Investigation (structural characterization, Sec.3.1), Validation, Visualization, Writing, Supervision, Resources, Project administration, Funding acquisition.

Contributions

Victoria M. Wu performed and conducted the performance of biological assays and managed the research space. M. K. Ahmed and Mervat S. Mostafa performed ab initio analyses and interpreted them with the assistance of Vuk Uskoković. Vuk Uskoković performed and directed the synthesis and characterization of the materials, conceptualized and supervised the project, and wrote the paper.

Conflicts of interest

There are no conflicts of interest to declare.

It also increased the roughness of the material in direct proportion with the content of the selenite dopant, thus having a potentially positive effect on cell adhesion and integration with the host tissue. Selenite in total acted as a crystal structure breaker, but was also able to bring about symmetry at the local and global scales within specific concentration windows, indicating a variety of often mutually antagonistic crystallographic effects that it can induce in a concentration-dependent manner. Experimental determination of the lattice strain coupled with *ab initio* calculations on three different forms of carbonated HAp (A-type, B-type, AB-type) demonstrated that selenite ions initially substitute carbonates in the crystal structure of carbonated HAp, before substituting phosphates at higher concentrations. The most energetically favored selenite-doped HAp is of AB-type, followed by the B-type and only then by the A-type. This order of stability was entailed by the variation in the geometry and orientation of both the selenite ion and its neighboring phosphates and/or carbonates. The incorporation of selenite also led to a variation of different thermodynamic parameters, including entropy, enthalpy, heat capacity and the Gibbs free energy in different types of carbonated HAp. Solubility of HAp accommodating 1.2 wt.% of selenite was 2.5 times higher than that of undoped HAp and the ensuing release of the selenite ion was directly responsible for inhibiting RAW264.7 osteoclasts. Dose-response curves demonstrated that the inhibition of osteoclasts was directly proportional to the concentration of selenite-doped HAp and to the selenite content in it. Meanwhile, selenite-doped HAp had a significantly less adverse effect on osteoblastic K7M2 and MC3T3-E1 cells than on RAW264.7 osteoclasts. The therapeutically promising osteoblast vs. osteoclast selectivity of inhibition was absent when the cells were challenged with undoped HAp, indicating that it is caused by selenite ions in HAp rather than by HAp alone. It is concluded that like three oxygens building the selenite pyramid, the coupling of (1) experimental materials science, (2) quantum mechanical modeling and (3) biological assaying is a triad from which a deeper understanding of ion-doped HAp and other biomaterials can emanate.

Keywords

Ab initio; Calcium phosphate; Hydroxyapatite; Nanoparticles; Osteoblasts; Selenite

1. Introduction

Hydroxyapatite (HAp) is known for a plethora of peculiar properties[1], one of which is the ability to undergo exceptional lattice strains to accommodate foreign cationic and anionic species in place of one or more of its ionic constituents: Ca^{2+}, PO_4^{3-} and OH^-. Recently, it was shown that 90 % of the naturally occurring and nonradioactive elements with atomic numbers from 1 to 83 have been stably accommodated inside the HAp lattice[2]. Ions as light as lithium[3] and boron[4] and as heavy as bismuth[5], uranium[6] and plutonium[7] were successfully incorporated into HAp, with secondary phases usually detectable only at excessively high concentrations of the foreign ion. As a result, doping with single or multiple ions has become one of the mainstream approaches to endowing HAp with new properties or augmenting the preexisting ones[8,9,10]. Biogenic apatite, in fact, owes its ability to act as a mineral reservoir and heavy metal depository for the body to this fundamental crystallographic and stoichiometric flexibility. At the same time, replacing small molecule and biologic drugs as traditional pharmacotherapies with therapeutically effective ions

presents a potentially prolific direction of research in biomedical sciences, primarily because a number of side effects of the former compounds - such as the proneness to elicit resistance of the pathological cells or tissues to chemotherapy and the risk of slow clearance and toxic accumulation in liver, spleen and other organs - could be avoided with one such approach. Whether its therapeutic prospect matches in scope that of the traditional drugs is debatable, but its prophylactic potentials are indisputable. When their low cost, affordability and synthetic ease and reproducibility are added to the equation, the ion delivery approach may prove to be commercially viable and clinically available in the near future.

While most ionic substitutes in HAp experimented with so far in search of a perfect ionic combination have been cationic, their usually lesser atomic weight, higher diffusivity and lesser residence time on surfaces makes them less stably interactive than anions. Anions are for this reason known to affect surface growth more intensely and selectively than cations[11]. Also, while Ca^{2+} and most cations partially substituting it in biogenic apatite, *e.g.*, K^{+}, Na^{+} and Mg^{2+}, lie on the chaotropic end of the Hofmeister series[12], PO_4^{3-} lies on the opposite, kosmotropic end, implying that its substitution should potentially have a more organizational than disorderly effect on bone. Yet another argument in favor of anionic substitutions is that relocation of Ca^{2+} from bone to organs such as brain, heart and kidney during the course of one's lifetime causes the deficiency of this ion in bone and the loss of bone mass, making it more prone to fracture. In contrast, phosphate deficiency is not only much rarer and usually tied to genetic pathologies[13], but it has also not been linked to bone weight loss. With 99 % of bodily calcium and 85 % of bodily phosphate residing in bone, the homeostasis of the latter ion is more broadly distributed and implies that its abrupt drops in concentration in critical organs will have a lesser effect on bone density.

Selenium is an essential trace element and although it does not exceed 0.1 % of the body weight[14], it exhibits a number of positive effects on human health[15]. It is an elemental component of several selenoproteins, including enzymes, most notably those from the antoxidant families of glutathione peroxidases and thioredoxin reductases[16,17]. As a part of these enzymes, selenium can mitigate the oxidative stress induced by heavy metals[18], thanks to which it has a protective effect against a number of diseases, including Alzheimer's[19] and cardiovascular[20]. Selenium deficiency is also known to negatively correlate with the neonatal brain development[21]. In fact, clinical studies have shown that its deficiency predisposes humans to 40 different diseases[22] and agricultural plants have started to be grown in seleniferous soils to cope with the global problem of the nutritional deficiency of selenium[23]. Selenium is also used in medical instrumentation, with one example being the use of amorphous selenium (α-Se) as a detector of radiation in the imaging technologies, such as X-ray computed tomography[24]. In our former study we discovered an array of benefits consequential to doping HAp with selenium oxyanion, SeO_3^{2-}, including the endowment of HAp with antibacterial, anticancer and osteoinductive properties thereby[25]. Selenium is known to benefit bone health as a dietary micronutrient, but the exact cause of this therapeutic effect has not been pinpointed. Its deficiency is known to inhibit new bone growth[26] and disrupt the healthy bone microarchitecture[27], while intake as a dietary supplement can restore the osteoporotic bone to a normal density[28]. Likewise, its use as a drug delivery carrier alleviated the adverse effect of bone resorption caused by the drug, anastrazole, itself[29]. In this study we continue the elucidation of structural effects of selenite

incorporation into the HAp lattice and also explore the possible effect of selenite-doped HAp (Se-HAp) on the inhibition of osteoclastic cells. HAp, itself, is known for pronounced osteoconductivity and occasionally exhibited osteoinductivity, as indicated by its ability to augment the osteogenic activity of osteoblasts[30]. Its effect on osteoclasts has, however, not been optimized yet through compositional or structural modifications for the osteoclastic inhibition and the use of therapeutic ions for such ends presents a logical approach. However, since the compositional modification of HAp can cause structural changes and, thus, affect its biological response, both of these effects must be explored as a function of the concentration of the foreign ionic specie. One such analysis of physicochemical and biological properties of HAp at different concentrations of the selenite anion incorporated in the material, ranging from 0.1 to 3.0 wt.%, was performed in this study.

Osteoporosis is a systemic bone disease typified by the imbalanced metabolic activity of the two types of mutually antagonistic bone cells: bone-building osteoblasts and bone-lysing osteoclasts[31]. It is a disease that strikes more than half of women older than 50[32] and is responsible for bone fractures experienced by 1 in 3 women and 1 in 5 men over the age of 50[33]. As such, it is in need of more precisely localized therapies than the systemic ones that are in use today or the preventive ones, *e.g.*, vitamin D, that often have no effect[34]. A typical pharmacotherapy against osteoporosis includes estrogen or bisphosphonates, compounds known for an array of adverse side effects[35]. Multiple anabolic agents have been developed as alternatives to bisphosphonates, including parathyroid hormone-related protein analogs[36], monoclonal antibodies against sclerostin[37] and cathepsin K inhibitors[38]; however, the challenges of delivering them efficiently and without compromising the body's natural bone remodeling cycle remain. By potentially inhibiting the metabolic activity and differentiation of osteoclasts and at the same time augmenting the new bone formation by osteoblasts, the medical relevance of Se-doped HAp becomes obvious. Testing this inhibition in osteoclastic RAW264.7 cells relative to the effect on osteoblastic K7M2 and MC3T3-E1 cells presents the objective of the biological segment of this study.

2. Experimental

2.1. Synthesis of HAp and selenite-containing HAp

To synthesize HAp, 88 ml of 0.1 M calcium nitrate, $Ca(NO_3)_2$, and 94 ml of 0.06 M ammonium hydrogen phosphate, $(NH_4)_2HPO_4$, were mixed and 18 ml of 1 M ammonia, NH_4OH, was added to the reaction mixture, which was then heated to 65 °C and maintained for an hour. To make Se-HAp with different selenite contents, different amounts of sodium selenite, Na_2SeO_3, were added to the $(NH_4)_2HPO_4$ solution (Table 1). The formed suspension was allowed to cool at room temperature, before being washed with deionized water. Prior to washing and after washing, the precipitate was separated from the supernatant by centrifugation at 5000 rpm for 5 minutes. The precipitate was then dehydrated overnight in a vacuum oven at 80 °C. The dried powders were divided to two groups: one group was used as-prepared and another group was annealed at 800 °C for 3 h in a horizontal tube furnace (Acros International, STF1200) in air.

2.2. Physicochemical characterization

X-ray diffractometry was carried out on a Bruker D2 Phaser diffractometer and on as-precipitated and annealed powders in the 10 – 90 ° 2θ range, with the step size of 0.002° and the scan time of 1.5 seconds per step. The diffraction peak analysis was performed by calculating a background function and deconvoluted peak profile using an automated Gaussian-fitting routine (*OriginPro 2016*). Interplanar spacing (d_{hkl}) was measured using the Bragg relation where λ is the wavelength of Cu K_α radiation, 1.5418 Å, and θ is the diffraction angle for (hkl) reflection:

$$d_{hkl} = \frac{\lambda}{2sin\theta_{hkl}} \quad \text{(Eq. 1)}$$

The hexagonal lattice parameters of HAp, *a* and *c*, were calculated from d_{hkl} using the following equation:

$$\frac{1}{d^2} = \frac{4}{3}\left(\frac{h^2 + hk + k^2}{a^2}\right) + \frac{l^2}{c^2} \quad \text{(Eq. 2)}$$

Williamson-Hall (WH) plots were constructed to differentiate the effects of the lattice strain from the effects of the crystallite size on the broadening of diffraction lines. (βcosθ)/λ was plotted as a function of d*, where β is the integral breadth calculated as a ratio of the integral area of a diffraction peak to its height, θ is the diffraction angle, and d* is the reciprocal Bragg distance, 1/d, corresponding to the given diffraction line. The following equation[39], where D is the average crystallite size and ε is the measure of the microstrain distribution, was used to derive the strain from the slope of the curve:

$$(\beta\cos\theta)/\lambda = D^{-1} + 2\varepsilon d^* \quad \text{(Eq. 3)}$$

To estimate the activation energy of crystallization of amorphous domains in HAp and Se-HAp, XRD patterns of as-precipitated powders and powders annealed at 200, 400, 600 and 800 °C for 2 h were compared for the integrated intensities of the (222) reflection at 2θ = 46.7 °. The Avrami expression for solid state transformations is given as Eq.4, where *x* is the transformed material fraction after time *t*, *n* is the dimensionless Avrami constant and *k* is the reaction rate constant calculable from the temperature-dependent Arrhenius equation (Eq.5), where k_o is a standard rate constant, E_a is the activation energy (kJ/mol), *R* is the gas constant (8.3145 J/kmol) and *T* is the temperature (K)[40]:

$$x = 1 - e^{-(kt)n} \quad \text{(Eq.4)}$$

$$k = k_o e^{-Ea/RT} \quad \text{(Eq.5)}$$

By substituting *k* from Eq.4 in Eq.5, an expression is derived, from which E_a can be determined as the slope of the linear fit of the plot of ln[−ln(1 − x)] vs. 1/T. To determine the

crystallization extent, *x*, the integrated intensity of the (222) reflection after annealing at 800 °C was taken as a 100 % value and the corresponding intensity in an as-precipitated sample was taken as a 0 % value. The parameter *x*, itself, had values in the 0 – 1 range.

Fourier transform infrared spectroscopy (FTIR) was used to additionally follow the effects of selenite substituent at various concentrations, and the analysis was done on a Bruker Alpha Platinum ATR spectrometer. Transmission Electron Microscopy (TEM) studies were performed on a JEOL JEM 1220 Life Science TEM operated at 80 kV. Field Emission Scanning Electron Microscopy (FE-SEM) studies were carried out on an FEI Magellan 400 SEM operated at 30 kV voltage and 25 μA beam current. Sample preparation involved depositing powders with spatula on clean aluminum stubs using carbon tape and subsequently sputter-coating them (Leica 600) with iridium up to the thickness of 3 nm to reduce the surface charging effects. FE-SEM images were processed using Gwyddion 2.45 freeware[41]. Three-dimensional graphs were created for each sample at the resolution of 1450 × 950 pixels and the roughness parameters were computed in nm units. Inductively Coupled Plasma Mass Spectroscopy (ICP-MS) analysis was performed to measure the exact amount of selenite ions per weight of apatite in Se-HAp samples (Table 1). This analysis was carried out on a PerkinElmer NexION 350D ICP-MS in the Microanalysis laboratory at University of Illinois at Urbana-Champaign. Prior to the analysis, the samples were dissolved in 1 M HCl and diluted to below 80 ppb.

Calcium release analyses were done by immersing 10 mg of powders in 10 ml of 20 mM Bis-Tris aqueous solution (pH 6.8) and measuring the solution potential using the Ca^{2+} microelectrode in combination with a reference electrode (*Microelectrodes, Inc.*) plugged to a regular pH-meter (*Fisher Scientific*). Calibration solutions were prepared in the same solvent and using $CaCl_2$ in the 1 μM – 100 mM concentration range. Calibration data points were exponentially fitted in the 1 μM – 1 mM $CaCl_2$ (*OriginPro 2016*) and the numerical fit was used to convert the electrode potential readings into free Ca^{2+} molar concentrations. All the samples were analyzed in triplicates and compared against the control samples.

2.3. Ab initio calculations

Calculation of the most stable structure of carbonated HAp doped with SeO_3^{2-} was carried out using CASTEP code based on *Ab initio* quantum mechanical computations in Materials Studio 6.0 [27]. All runs were carried out under the same conditions: express quality, the gradient approximation GGA, SCF tolerance of 10^{-4} eV/cell, the maximum force of 100 eV/Å, the maximum stress of 100 GPa, the maximum displacement of 100 Å. Convergence was done with the cutoff energy of 340–370 eV. K-point set (3×3×4). The minimization algorithm used to minimize the energy was Broyden– Fletcher–Goldfarb–Shanno (BFGS). Thermodynamic parameters including entropy, enthalpy, heat capacity and the Gibbs free energy, along with the IR bands, were computed using the DMol3-GGA-PBE function. The calculations were carried out with a coarse integration accuracy. The effective core potentials were taken into consideration with the basis set of DN.

2.4. Cell culture and osteoclastic differentiation

Mouse monocyte macrophage RAW264.7 cells were obtained from American Tissue Culture Collection (*ATCC*, Rockville, MD) and cultured in Dulbecco's modified Eagle medium (DMEM) with 10 vol.% fetal bovine serum and 5 vol.% amphotericinB (streptomycin/penicillin/fungisone) as the antibiotic/antimycotic. To differentiate them into an osteoclast-like phenotype, they were seeded at 1.5×10^5 cells/well in 24 well plates and incubated for 7 – 9 days in the medium additionally containing 35 ng/ml RANKL/TRANCE (*R&D system*). The medium was replaced every other day and differentiated, large multinucleated cells could be seen in the wells by Day 5. On Day 7, the cells were stained for Tartrate-resistant acid phosphatase (TRAP) as an osteoclast marker using a commercial acid phosphatase leucocyte kit (*Sigma*).

K7M2 murine osteosarcoma cells were purchased from *ATCC* and were seeded at 5,000 cells/well in Falcon 96-well plates and allowed to incubate for 48 h prior to administration of the nanoparticles. Mouse calvarial preosteoblastic cell line, MC3T3-E1 subclone 4, was purchased from ATCC and cultured in Alpha Minimum Essential Medium (α-MEM; *Gibco*) supplemented with 10% fetal bovine serum (*Invitrogen*) and no ascorbic acid. The medium was replaced every 48 h, and the cultures were incubated at 37 °C in a humidified atmosphere containing 5% CO_2. Near confluence, cells were treated with 5 mg/ml of HAp or Se-HAp particles and 50 μg/ml ascorbic acid as the mineralization inductor in MC3T3-E1 cells, and incubated for 48 h.

2.5. MTT cell viability assay

MTT (3-(4,5-Dimethylthiazol-2-yl)-2,5-Diphenyltetrazolium Bromide) solution was prepared according to the manufacturer's instructions (Vybrant® MTT Cell Proliferation Assay Kit V-13154). Cells were plated as described previously, cultured until confluency and challenged with 1, 2 or 5 mg/ml of Se-HAp nanoparticles and incubated for 48 h at 37 °C with 5% CO_2. The assay was performed according to the manufacturer's instructions and absorbance was measured at 540 nm using a microplate reader (FLUOstar Omega, BMG LABTECH). To circumvent the aggregation issues, only as-precipitated, non-annealed Se-HAp particles in suspension were used in biological assays.

2.6. Cell/nanoparticle visualization

RAW264.7 cells seeded in coverslips laid at the bottoms of the 24-well plates were differentiated for 7 days in media containing 1 mg/well of Se-HAp nanoparticles. Cells on coverslips were then first washed with 1x phosphate buffered saline (PBS) to remove the nanoparticles that had not been endocytosed, then fixed for 5 minutes in 4 wt.% paraformaldehyde, then washed with 1x PBS and incubated in the dark for 30 minutes with Alexa Fluor 568 Phalloidin (1:400) (*Molecular Probes*) to stain f-actin filaments and OsteoImage™ (*Lonza*) to stain Se-HAp particles. After the incubation, the coverslips were rinsed in 1x PBS and washed in the dark for 3 × 5 minutes in 1x PBS. Cell nuclei were then stained using NucBlue fixed cell ReadyProbe reagent (*Molecular Probes*) for 20 minutes. Images were acquired on a Zeiss LSM 710 confocal microscope.

3. Results and discussion

3.1. Structural insights through physicochemical characterization

Correlation between selenite and carbonate can be instructive in the attempt to understand the accommodation of selenite into the structure of HAp. Compared to phosphate tetrahedron, selenite, SeO_3^{2-}, is a pyramidal oxyanion structurally analogous to carbonate, CO_3^{2-}, the most dominant ionic substitute for phosphates in biogenic apatite[42]. Namely, the average content of carbonates in bone mineral is 3 – 8 wt.%, exceeding the amount of all cationic dopants combined (~ 1 – 2.5 wt.%)[43]. On the basis of charge neutrality, the chemical formula of Se-HAP is similar to that including CO_3^{2-} ions[44]: $Ca_{10-x/2}[(PO_4)_{6-x}(CO_3)_x][(OH)_{2-2y}(CO_3)_y]$, where x and y are numbers of SeO_3^{2-} ions substituting for PO_4^{3-} and OH^-, respectively. The thermochemical radii of divalent selenite and trivalent phosphate ions are highly similar, 239 and 238 pm, respectively, indicating a minimal atomic volume effect on the lattice strain caused by this substitution *per se*. The largest contribution to the lattice strain, as seen from Fig.1, in fact, is thought to come from the dual calcium and hydroxyl site vacancies created to compensate the charge imbalance resulting from the substitution of trivalent phosphate with divalent selenite. This loss of hydroxyl groups is typically seen in biogenic apatite too as the result of the accommodation of carbonate ions, with the hydroxyl content in it ranging from approximately one tenth to one third of the stoichiometric amount[45,46]. A less commonly observed stoichiometric effect occurring instead of the loss of hydroxyls and accompanying the formation of calcium vacancies is that of the partial retention of divalent, the most physiologically stable phosphate specie, HPO_4^{2-}, in the lattice of HAp.

Morphological analysis carried out using the FE-SEM demonstrated a more anisotropic growth of HAp nanoparticles as the result of the phosphate-to-selenite substitution, even at the lowest selenite weight content of 0.1 wt.%, where only one in ~ 500 phosphate groups would be substituted by selenite. Thus, based on the FE-SEM images, pure HAp was composed of conglomerates of round- and rod-shaped, narrowly dispersed, 20 – 100 nm sized particles (Fig.2a). The addition of selenite led to the formation of plate-shaped particles that were also considerably larger: ~ 300 nm on average along their longest axis. While these plate-shaped particles were distinct at the lowest, 0.1 wt.% content of selenite (Fig.2b), their merging into indistinct, coral-shaped aggregates became evident at higher selenite contents (Fig.2c). Amorphization of HAp is characterized by the progressive increase of such indistinct, gelatinous flocculate domains that radiate outwardly as bud-like extensions from discoid particles[47,48], such as those visualized in Fig.2b–c. The topographic analysis of Se-HAp surfaces at different selenite contents corroborated the sharpening of surface features in direct proportion with the concentration of selenite in the particles (Fig.2d–f). The average roughness of the surface composed of compressed particle conglomerates correspondingly increased from 25.3 nm in pure HAp to 28.9 nm in Se-HAp containing 0.1 wt.% of selenite to 31.3 nm in Se-HAp containing 1.2 wt.% of selenite, and the root mean square roughness followed the same trend (Table 2). Surface roughness, such as that caused by the scratches on overused magnetic stir bars, the common foreign agents in chemical reaction vessels, can increase the activity of inorganic species[49], but it can also increase the metabolic activity of cells binding to such surfaces, including fibroblasts[50],

osteoblasts[51] and osteoclasts[52]. Therefore, this increased roughness accomplished by the integration of selenite into HAp is expected to facilitate cell adhesion and also augment the implant/bone union, given that surface roughness usually enhances osseointegration[53]. In addition to increasing surface roughness by particle elongation effects, selenite based on FE-SEM imaging also induces lattice distortions, which decrease the surface free energy[54] and may positively affect the chemical interaction with the host surface.

HR-TEM analysis corroborated the FE-SEM data by demonstrating a similar elongation of the initially rod-shaped HAp particles upon the addition of selenite (Fig.2d,g). Simultaneously, the concentration of amorphous domains increased and the concentration of crystalline, lattice-fringed domains decreased in HAp rods as selenite ions were incorporated into them (Fig.2e,f). An increase of the particle size and the adoption of more complex morphological symmetries on one hand and a parallel increase in the presence of the amorphous domains in the powder on the other hand suggest a dual influence of selenite on the structure of HAp. While the former effect will turn out to be dominant at lower selenite contents, the latter effect will take over the influence over the structure of Se-HAp at higher selenite contents. Based on the defect-inducing effect of selenite schematized in Fig.1, it can be assumed that selenite *per se* promotes the crystal growth in concert with the hexagonal symmetry habit, but it also creates defects whose multiplying eventually disorders the lattice, thus indirectly amorphizing the structure. Tied to calcium ion vacancies, this effect can be considered central in explaining the structural disorder caused by phosphate-to-selenite substitution. Still, the contribution of the selenite ion to distortion of the phosphate network, which is often considered most critical for the preservation of structural order in HAp[55,56], should not be neglected.

To understand the structural effects of selenite oxyanion on HAp, a crystallographic analysis was conducted on the annealed powders and lattice parameters were calculated from diffraction line angles and intensities. As seen in Fig.3a, at low concentration of selenite, its presence lowered the crystallinity isotropically, by expanding the lattice in both the direction of *a* and *c* axes. At higher concentrations, the effect was opposite and more intuitive given its lower size and charge compared to the phosphate ions that it presumably substitutes for. Namely, its inclusion is expected to lead to the creation of coupled calcium and hydroxyl vacancies and result in moderate shrinkage of the lattice. This effect is indeed seen at the highest concentration of selenite, at which the lattice strain becomes negative in both [001] and [hk0] directions, indicating the isotropic lattice contraction (Fig.3a). At the same time, the crystallite size, which initially, at low concentration of selenite, dropped isotropically, decreased along the basal plane and increased along the screw axis, suggesting the extension of the crystallites along the most logical, *c* axis, albeit to a moderate extent, by mere 11 % at the highest concentration of selenite compared to undoped HAp (Fig.3b). This effect, which has clear morphological corollaries (Fig.2), is analogous to the contraction of the *a*-axis and the expansion of the *c*-axis, accompanied by a decreased crystallite size and an increased lattice strain, resulting from carbonate-to-phosphate substitution in HAp lattice[57,58]. Hence, the decrease in the crystallite dimensions along the *a* axis is approximately compensated by the increase in the crystallite dimensions along the *c* axis in as-precipitated, non-annealed Se-HAp. This concentration-dependent effect that the selenite ion induces in the structure of Se-HAp indicates the complex rearrangements within and beyond the limits of the unit cell

that entail this form of doping. It is also in agreement with the previously evidenced concentration-dependent variations in the lattice parameters *a* and *c* caused by the structural integration of selenite[59,60]. A previous study on the sorption of selenite onto HAp[61] showed a similarly isotropic expansion of the lattice at these comparatively low substitution rates, while another study[62], involving the bulk capture of the selenite ion and implying higher substitution rates, reported an isotropic contraction of the lattice, like the one detected here at higher selenite concentrations.

That the changes to crystallographic properties are not due to the lowering of the crystallite dimensions in proportion with the amount of selenite ions, but due to their effect on increasing the lattice strain can be observed from the corresponding roentgenograms, showing the consistent narrowing of the (222) diffraction peak and an increase in the noisy component of the pattern entailing the successive increases in the amount of selenite ions incorporated in the lattice (Fig.4a–b). This high index plane, (222), was selected for estimation of the averaged crystallite domain dimensions because of its diagonal nature, cutting through the lattice with no preferential axial direction, but also because of its lack of diffraction line overlap, unlike that present for the most intense, (211) reflection at 2θ = 31.86 ° overlapping intensely with (112) at 2θ = 32.20 ° and moderately with (300) at 2θ = 32.90 °. Whereas the halfwidth of this high index plane increased for the as-prepared samples in proportion with the amount of selenite incorporated into the lattice (Fig.4a), indicating the lowering of the crystallite domain size, the effect was opposite for the thermally treated samples (Fig.4b), in spite of the noisy fingerprint of the patterns increasing with the selenite content and indicating a parallel increase in the lattice strain. Applying the Scherrer equation to the halfwidth of the (222) reflection in the selenite-free HAp indicated the average crystallite size of 32.4 nm, but this value increased beyond the 100 nm range of the validity of this equation[63] in parallel with an increase in the selenite content and these values are, therefore, not reportable.

The increase in the integrated intensity of the (222) reflection with the annealing temperature, however, allowed for the activation energy (E_a) for the crystallization of amorphous domains in poorly crystalline HAp and Se-HAp precipitates to be calculated. The values shown in Table 3 demonstrate a consistent increase in E_a with the amount of selenite integrated into Se-HAp, the reason for which are twofold. First, with the reduction of crystallinity in direct proportionality with the amount of selenite in Se-HAp, a greater amount of energy must be invested to induce lattice reordering during the recovery. Second, the addition of selenite increases the average particle size, thus lowering the specific surface area (S_a) of the material, which is usually inversely proportional to the crystallization rate. Eq.6 gives the theoretical basis for the inverse relationship between S_a and E_a[64]. Specifically, it shows the direct correspondence between the radius of the spherical nucleus of a new phase crystallizing from a melt, R_c, and E_a for nucleation in the condensed phase, where w is the frequency of the addition of the growth units of the crystallizing material to critical nuclei in s^{-1}, K_n is the coefficient of proportionality involving steric factors (the probability of achieving the correct orientation of the growth units), a is the mean free path of diffusion, f_0 is the frequency of thermal vibrations of the growth units comprising the crystallizing material in s^{-1}, and n^* is the concentration of the growth units in the supersaturated mother phase in m^{-3}:

$$R_c^2 = w\exp(E_a/2RT)/4\pi K_n n * af_0 \quad \text{(Eq.6)}$$

By taking into account that S_a is inversely proportional to R_c, it can be concluded that E_a, in theory, should be also inversely proportional to S_a. A similar relationship was reported earlier for the crystallization of thermally treated amorphous silica gels[65]. The semipermeable interface model of the scaled particle theory offers another framework for deriving the same relationship[66]. As per this theory, the following expression applies, where 1/(1+k) is the rate reduction factor, S_a is the total surface area and S_{a0} is the surface area available for hydroxyl ion binding:

$$1/(1 + k) = S_{a0}/S_a \quad \text{(Eq.7)}$$

To measure the effect of intracrystalline selenite accommodation on the lattice strain, Williamson-Hall plots were constructed involving the complete range of both low and high index planes. Lattice strain was not directly derivable from the plots in terms of absolute values, but the slopes of the linear fits, directly corresponding to the level of the internal strain, enabled the comparison between pure HAp and HAp doped with different amounts of selenite ions. Thus, the lattice strain evidently increased in parallel with an increase in the amount of selenite for both as-precipitated and annealed samples, although the effect was more discernable in the latter (Fig.5). As for the former, the strain increased with the addition of selenite to HAp in the amount of 1.2 wt.%, but then decreased with the further addition (Fig.5a), possibly because the increasing amorphization transformed solid pockets within the material from the intensely strained apatite to completely amorphized, non-apatitic structure which, together with the expansion of the internally confined amorphous regions to the particle surface, relaxed the lattice and lowered the effective strain. In contrast, the strain in the annealed samples increased at a steady rate in parallel with the addition of selenite (Fig.5b). A comparison between the non-annealed and annealed HAp samples at identical selenite contents shows that for lower selenite contents, the thermal treatment managed to lower the lattice strain through ionic diffusion. The same effect was, however, not observed for higher selenite contents, specifically 3 wt.%, in which case annealing increased the strain in spite of the formation of the secondary phase. The cause behind this phenomenon is thought to lie in the intergranular shear interactions. That a precisely tuned duration of the thermal treatment can cause strain relief, whereas prolongation of this treatment can increase the strain has been well-known in the literature[67]. The lattice strain is a direct result of the dominant defect formation mechanism employed to compensate the charge imbalance caused by the substitution of trivalent phosphates by divalent selenites. As depicted in Fig.1, this mechanism involves the formation of coupled calcium and hydroxyl vacancies, which produces various types of dislocations in the lattice. At higher selenite contents, reaching 3 wt.%, the amount of calcium vacancies becomes too abundant for calcium ions to be sustained in the lattice. This results in the formation of a low Ca/P molar ratio phase, specifically calcium pyrophosphate (Ca/P = 1 compared to 1.677 for HAp). This phase, which normally forms during the calcination of low Ca/P ratio CP phases, such as brushite or monocalcium phosphate, forms solely as the result of the coupled hydroxyl and

calcium vacancies forming to compensate the charge imbalance accompanying the selenite-to-phosphate substitution.

The FTIR analysis of the effect of the selenite ion incorporation into HAp at different concentrations confirmed the antagonistic effects on the crystalline order exhibited by this oxyanion at low and high concentrations. Namely, while the addition of selenite up to 1.2 wt.% increased the intensity of all four major phosphate vibration modes, exceeding this limit produced a contrary, disordering effect, as insinuated by the progressive drop in the band intensities in the 1.2 – 3 wt.% range of selenite contents (Fig.6a). The latter effect was observed earlier[68] and it confirms the role of selenite as a structural disruptor in HAp, as in agreement with its being causative of reduced crystallinity in HAp at comparatively high concentrations (Fig.4). However, at low concentrations, up to 1.2 wt.%, selenite exhibited an ordering effect, as all the major phosphate bands increased in both integrated and absolute intensities compared to undoped HAp (Fig.6c). This effect, however, became reverted once the selenite content exceeded this amount and the long-range symmetry began to rapidly decrease, leading to the gradual diminishment of the phosphate band intensities. Opposing this trend, the antisymmetric stretch, ν_3(P-O), of the selenite ion, its most intense band, was detected at 754 cm^{-1} and increased in parallel with an increase in the concentration of this ion in HAp (Fig.6c). Meanwhile, in spite of the increase and then a drop in the band intensities, the phosphate band halfwidths did not change depending on the selenite concentration, whereas the halfwidth of the major selenite vibration mode, ν_3(Se-O), decreased as the amount of selenite in the material increased (Fig.6d), indicating the increase in the stereochemical symmetry level around the selenite oxyanion in direct proportion to its concentration, as in agreement with the trend applying to band intensities (Fig.6c). Hence, the production of order in the short-range environment surrounding selenite pyramids was compensated by disordering the environment around the phosphate tetrahedra and came at the cost of the increased entropy of the total structure. Meanwhile, no frequency shifts in any of the major phosphate vibration modes were detected depending on the selenite concentration except for the antisymmetric, ν_3(P-O) stretch, which exhibited a significant blue shift, from 1023.97 to 1044.37 cm^{-1}. The successive ordering and disordering effect was detected with respect to both the phosphate vibration bands of HAp and the stretch of the hydroxyl ion confined to the channel extending down the rotational symmetry axis of $P6_{3/m}$ hexagons formed by the hexagonal, Ca2 ions. This confinement of the hydroxyl ions to the hexagonal channel of the unit cell and the resulting precise translational symmetry of their spatial arrangement is reflected in the comparatively sharp OH^- ion stretch with the maximum detected at 3570 cm^{-1} (Fig.6b). For this sharp absorption to occur, the lattice need not adopt the highest possible symmetry, monoclinic $P2_{1/b}$, which is typified by the aligned, unidirectional orientation of the proton of the hydroxyl groups per channel (all up or all down) and which transitions to the randomized orientation of the hexagonal, $P6_{3/m}$ space group in the presence of ionic substitutes or vacancies at concentrations lower than 10 %[69]. Although the band becomes sharper and more intense at low selenite dopant concentrations, it virtually disappears once the selenite content exceeds a certain threshold, suggesting the amorphization of the HAp lattice. The maximum of the symmetrical carbonate stretching mode, ν_1, was detected at 1087 cm^{-1}, which indicated the presence of the B-type HAp, in

which carbonates, competing with selenite, substitute for phosphate ions, not OH^- ions (A-type), for which this band would have been upshifted[70] to ~ 1100 cm^{-1} (Fig.6a).

The local minima in the lattice constants (Fig.3b) and the lattice strain determined by both the diffraction line broadening (Fig.3a) and the Williamson-Hall relationship (Fig.6) can be explained by the competition of selenite and carbonate pyramids for the same phosphate tetrahedron during co-precipitation of Se-HAp under ambient conditions (Fig.7) or, in other words, by the partial substitution of carbonate for selenite during precipitation of Se-HAp. To illustrate this effect in stoichiometric terms, the chemical formula of Se-HAp was supposed to be $Ca_x(PO_4)_{6-y}(SeO_3)_y(CO_3)_z(OH)_{2x+y-18-2z}$, $0 < x < 10$, $0 < y < 0.1$, $0 < z < 0.1$[71]. Precipitation of HAp under ambient conditions captures atmospheric carbonate ions present in water as the result of $CO_2 + H_2O \leftrightarrow 2H^+ + CO_3^{2-}$ equilibrium under alkaline conditions. The typical amounts of carbonate in such precipitates range from 0.5 to 1 wt.%[72,73], even though they can reach 8 wt.% by controlling the preparation conditions[74]. Carbonates have the affinity for both phosphates and hydroxyls in the structure of HAp, but $PO_4^{3-} \rightarrow CO_3^{2-}$ substitution, yielding B-type carbonated HAp, is most probable under ambient conditions, whereas the $OH^- \rightarrow CO_3^{2-}$ substitution, yielding A-type HAp, requires elevated temperatures[75,76]. With the thermochemical radius of selenite (239 pm) being more similar to that of the phosphate ion (238 pm) than to that of the carbonate ion (178 pm), it can be expected that $CO_3^{2-} \rightarrow SeO_3^{2-}$ substitution would lower the lattice strain resulting from the prior $PO_4^{3-} \rightarrow CO_3^{2-}$ substitution. Because the carbonate content can be estimated at ~ 1 wt.%, the minimal lattice strain coinciding with selenite contents of 1 – 2 wt.% suggests that selenite ions first replace carbonates, thus lowering the lattice strain brought about by $PO_4^{3-} \rightarrow CO_3^{2-}$ substitution, before replacing phosphates, thus contributing to a further increase in the lattice strain, presumably not so much because of the ion size discrepancy as because of the aforementioned charge imbalance reasons (Fig.1).

3.2. Structural insights through ab initio modeling

Ab initio investigation of selenite-substituted carbonated HAp was performed to better understand the structural effects of supplementation of HAp with selenite, particularly with respect to the hypothesized key role that structural carbonates play in accommodating selenite ions. Interaction of the selenite ion with three possible types of carbonate-containing HAp (cHAp) was examined using computational density functional theory: A-type where carbonate accommodates itself at the channel OH^- site, B-type where carbonate replaces the phosphate ion, and AB-type where carbonate occupies both of these positions[77]. A number of physicochemical properties are influenced by these substitutions and they all stem from the variations in the crystal structure[78], including the distortion of the unit cell owing to a change in the lattice parameters. Interestingly, while most studies on the accommodation of selenite in the crystal structure of HAp focused on pure HAp, no studies have been performed to understand the substitutions in cHAp, which is not only the natural product of the precipitation of HAp under ambient conditions, but also the major compositional feature of biogenic apatite. Namely, biological apatite contains a plethora of different cations (Mg^{2+}, Sr^{2+}, Fe^{2+}, Na^+, K^+, etc.) and anions (CO_3^{2-}, F^-, Cl^-, etc.) in addition to Ca^{2+} and PO_4^{3-}[79,80], with each of them playing a vital role in biological processes occurring in the bone[81] and with carbonate being the most prevalent foreign ion. Namely, CO_3^{2-} ions

represent 5–8 wt. % of biological apatite[82]. Since HAp acquires its importance mainly owing to its resemblance to the mineral part of human hard tissues[83], it is only logical to study its carbonated version. Although more compositionally similar to biogenic apatite, cHAp is, however, more complicated and challenging to analyze than pure HAp.

Based on the optimum geometries set previously[84], computation of the most energetically favored structure of cHAp doped with a predefined amount of SeO_3^{2-} ions was carried out. The monoclinic symmetry of the unit cell of HAp was assumed in order to cover all the lattice parameters, and three aforementioned types of cHAp – A, B and AB – were analyzed separately.

A-type cHAp was configured as $Ca_{10}(PO_4)_6CO_3^-$ and doping with selenite may involve the two following scenarios:

$$Ca_{10}(PO_4)_6CO_3 + (SeO_3)^{2-} \rightarrow Ca_{10}(PO_4)_5(SeO_3)CO_3 + (PO_4)^{3-} \quad \text{(Eq.8)}$$

$$Ca_{10}(PO_4)_6CO_3 + (SeO_3)^{2-} \rightarrow Ca_{10}(PO_4)_6(SeO_3) + (CO_3)^{2-} \quad \text{(Eq.9)}$$

The first scenario (Eq.8) assumes that selenite substitutes the phosphate group and accommodates itself on one of the six phosphate sites. Because there is one less structural oxygen anion per substitution and because of the inequivalent ways to configure the selenite pyramid, each phosphate group substitution includes four subcases, each referring to a different form of oxygen ion removal. Consequently, the first scenario contains 24 subcases. The second scenario (Eq.9) is equivalent to the simpler substitution of C^{4+} by Se^{4+} and can be covered in a single case.

B-type cHAp was arranged in the following formula: $Ca_9Na(PO_4)_5(CO_3)(OH)_2$. Note that out of the three types of cHAp, only B-type incorporates sodium ions as a mechanism for compensation of charge neutrality broken by the accommodation of divalent carbonates in place of trivalent phosphates and a calcium ion vacancy entailing this substitution. Sodium ions in this case originate from the dissociation of sodium selenite as the source of selenite ions during the synthesis of Se-HAp (see Sec.2.1). The other two types of cHAp, namely A and AB, give away monovalent hydroxyl groups upon the incorporation of carbonates, thereby creating a charge imbalance that could be compensated without variations in the Ca^{2+} ion positions. Considering this, there are two possible ways to accommodate selenite into B-type cHAp:

$$Ca_9Na(PO_4)_5(CO_3)(OH)_2 + (SeO_3)^{2-} \rightarrow Ca_9(PO_4)_4(SeO_3)(CO_3)(OH)_2 + (PO_4)^{3-} + Na^+ \quad \text{(Eq.10)}$$

$$Ca_9Na(PO_4)_5(CO_3)(OH)_2 + (SeO_3)^{2-} \rightarrow Ca_9Na(PO_4)_5(SeO_3)(OH)_2 + (CO_3)^{2-} \quad \text{(Eq.11)}$$

In the first scenario selenite substitutes a phosphate group and to preserve the charge neutrality, the process must be accompanied by a single oxygen ion removal. With five phosphate group positions and four oxygen ions available for removal in each position, the total number of subcases to be covered is 20. In each of these subcases, one sodium cation gets removed upon the accommodation of each selenite ion (Eq.10). The second scenario preserves sodium in the structure of cHAp, while selenite directly substitutes the carbonate ion (Eq.11).

AB-type cHAp contains two carbonate groups, one of which has replaced a phosphate group and the other one of which has replaced the hydroxyl ion. Here, there are three possible scenarios:

$$Ca_{10}(PO_4)_5(CO_3)_2(OH) + (SeO_3)^{2-} \rightarrow Ca_{10}(PO_4)_4(SeO_3)(CO_3)_2(OH) + (PO_4)^{3-} \quad \text{(Eq.12)}$$

$$Ca_{10}(PO_4)_5(CO_3)_2(OH) + (SeO_3)^{2-} \rightarrow Ca_{10}(PO_4)_5(SeO_3)(CO_3)(OH) + (CO_3)^{2-} \quad \text{(Eq.13)}$$

$$Ca_{10}(PO_4)_5(CO_3)_2(OH) + (SeO_3)^{2-} \rightarrow Ca_{10}(PO_4)_5(CO_3)(SeO_3)(OH) + (CO_3)^{2-} \quad \text{(Eq.14)}$$

The first scenario implies (Eq.12) the removal of one phosphate group per substitution, in which case the preservation of charge neutrality results in 20 subcases. The second (Eq.13) and the third (Eq.14) scenario assume the substitution of one of the two different carbonate ions in the unit cells of this type of cHAp with selenite ions, in which case the charge neutrality is not violated.

Evaluation of the most stable configuration involved the calculation of the defect formation energy ΔE_f as the difference between the energies of the defect-containing and the defect-free unit cells, as given in Eq.15, where E_{def} represents different types of cHAp doped with selenite, E_{undef} represents pure cHAp, n_i refers to the difference in the number of ionic species between the pure and defected unit cell, and μ_i denotes the chemical potential of ionic species approximated to the energy values at 0 K.

$$\Delta E_f = E_{def} - E_{undef} + \sum_{i=1}^{n} n_i \mu_i \quad (8) \quad \text{(Eq.15)}$$

Fig.8a shows the most stable structure of A-type cHAp before doping with selenite, while the most energetically favorable out of 25 calculated Se-doped A-type cHAp structures is shown in Fig.8b. Comparison between the undoped and doped A-type cHAp has indicated that the first scenario, where selenite substitutes phosphate (Eq.8), is preferred over the second scenario, where selenite substitutes carbonate (Eq.9). The unit cell suffered from

dramatic changes, such as doubling of the surface Ca^{2+} ions shared with the neighboring cells and the decrease of the number of carbonate ions in the unit cell to one half of its initial value. The final form of A-cHAp doped with selenite may deviate from the first scenario and adopt $Ca_9(PO_4)_5(SeO_3)(CO_3)_{0.5}$ stoichiometry, with the ΔE_f of 363.92 eV.

Lattice parameters for the pure and the doped structures are reported in Table 4. Small shifts occur in A-type cHAp due to doping with selenite, including the reduction of lattice parameters *a* and *b* by 1.31 % and 3.92 %, respectively, causing the unit cell volume to be contracted as a whole by 5.75 %. On the other hand, the lattice parameter *c* increased slightly. This reduction of the two basal plane lattice parameters and an expansion along the c-axis is in agreement with the same effect evidenced in the XRD analysis (Fig.3b). Owing to the difference in charge between selenite and phosphate, the Ca^{2+} ions redistributed to keep the neutrality, explaining the slight change in the lattice parameters. As seen from Fig.8c, P^{5+} ion formed a tetrahedron by coordination with 4 oxygen anions with the bond lengths of 1.535, 1.546, 1.544 and 1.530 Å. In selenite-doped A-type cHAp, these bonds got elongated due to the repulsion effect caused by the lone pair of Se^{4+} ions, reaching 1.772, 1.794 and 1.8442 Å (Fig.8d). Namely, the lone pair minimizes the size of the Se^{4+} ion, but at the same time it contributes to the repulsion between the lone and the bonding pairs of electrons, which becomes minimized by elongation of Se^{4+}-O bonds and a decrease in the P^{5+}-O bond angles. Because of this extension of selenite bonds and a reduction of P^{5+}-O bond angles, the size difference between selenite and phosphate becomes more pronounced than the minimal, 1 pm difference inferable from their thermodynamic radii: 2.39 $Å^3$ and 2.28 $Å^3$, respectively. However, the shape has been modified significantly due to the rearrangement of the oxygen ions around the center ion, where the column shape of the phosphate tetrahedron transformed to the flatter selenite pyramid.

The most stable unit cell conformation of B-type cHAp is illustrated in Fig.9a. In this case, the introduction of one carbonate ion expels one of the phosphate groups and the demand for the preservation of charge neutrality allows a monovalent cation such as Na^+ to substitute one of the constitutive Ca^{2+} atoms. The carbonate group is lying on the b/c plane and the stoichiometric configuration of B-type cHAp could be formulated as $Ca_9Na(PO_4)_5(SeO_3)(OH)_2$. The most stable unit cell of B-type cHAp accommodating selenite implies the ousting of the carbonate group because, as seen in Fig.9b, selenite substitutes the carbonate group. Due to the large difference in the ionic radii between Se^{4+} and C^{4+} (0.5 and 0.16 Å, respectively), the ionic bonds and angles change dramatically after the substitution, as is obvious from Fig.9c–d. The size of the carbonate group was ~ 1.78 $Å^3$ and the C^{4+}-O bond lengths in it equaled 1.290, 1.316 and 1.313 Å. In contrast, the $4sp^3$ hybridization with lone pair of electrons in selenite causes bond elongation based on previous arguments and transformation to 1.694, 1.696 and 1.730 Å, respectively. The orientation angles of the carbonate group decreased after the selenite substitution to compensate for the expansion of bond lengths. The number of surface Ca^{2+} ions per unit cell decreased from 10 before the substitution to 6 after it. Consequently, the second of the two outlined substitution scenarios (Eq.11), where selenite directly substitutes carbonate in the unit cell of cHAp, can be considered more probable in B-type cHAp. The calculated ΔE_f equaled −101.552 eV, which indicated the higher stability of the selenite dopant in B-type cHAp than in the A-type one. Due to the difference in size between CO_3^{2-} and SeO_3^{2-} ions, the unit cell has been

distorted significantly. The lattice parameters a, b, c and Ω increased considerably, by 3.15, 2.21, 1.04 and 3.83 %, respectively. The crystal angles also have been effected, including α and γ, which increased by 5.16 and 1.71 %, respectively, while β decreased by 5.85 %. The platelet carbonate transformed to the pyramidal shape of the selenite. As illustrated in Fig.9d, the selenite pyramid is oriented perpendicularly to the c/a plane, as the result of which β decreased while α and γ increased.

Fig.10a displays the most preferred structure for AB-type cHAp. This model is distinguished by the inclusion of two carbonate groups to the unit cell. One of these carbonate groups (C_{PO}) replaces a phosphate group and the other one (C_{OH}) occupies the hydroxyl position. The triangular C_{PO} is approximately parallel to the c-axis and lies on the b/c plane, while $C_{OH\ is}$ aligned with the screw axis. Selenite preferentially substituted $C_{PO,}$ inducing a dramatic change in the dimensions of the ionic group. Namely, the bond lengths equaled 1.290, 1.314 and 1.305 Å for the triangular C_{PO} and 1.678, 1.690 and 1.695 Å for the accommodated selenite group. The orientation angles decreased slightly compared to the substitution in B-type cHAp. Both carbonate and selenite adopted nearly platelet shapes. The number of surface Ca^{2+} ions in the unit cell decreased slightly after doping with selenite and ΔE_f equaled −103.661 eV, indicating a slightly higher level of stability than that achieved in B-type cHAp and a significantly higher one than that achieved in A-type cHAp. It is also clear that the first of the three possible scenarios (Eq.12), where selenite replaces phosphate and leaves the carbonate intact, is favored in this case. The lattice parameters a, b, c and Ω decreased by 0.46, 1.04, 1.67 and 3.37 %, respectively, while the angles α, β and γ increased by 0.14, 0.21 and 0.23 %, respectively, due to the addition of selenite.

A comparison of selenite geometries and orientations between the three different types of cHAp shows the following trend for the selenite ion expansion: AB > B > A. This expansion lessens the difference in the shape between carbonate and selenite ions by flattening the selenite pyramids and rendering them more plate-like in shape. The most favored structure, for this reason, assumed the most flattened of all the selenite ion geometries.

Ab initio calculated IR bands of selenite-doped cHAp are reported in Table S1. They are split into two parts: before and after the doping with selenite. Most remarkably, the A-type cHAp bands at 1517.3 and 1537.2 cm^{-1}, which are assigned to the antisymmetric ν_3 stretching mode of the carbonate ion, got shifted to lower and higher frequencies, respectively, whereas the antisymmetric ν_3 stretching mode of carbonate in B-type cHAp at 1522 cm^{-1} disappeared completely after the addition of selenite. This is in agreement with the fact that selenite from the theoretical standpoint most probably substitutes phosphate in A-type cHAp (Eq.8) and carbonate in B-type cHAp (Eq.11). Concerning selenite itself, its theoretically IR-active vibration modes are ν_3 and ν_4. The bands at 797.1, 820 and 827.3 cm^{-1} could be attributed to the asymmetric stretch (ν_3) of O-Se-O in A-, B- and AB-types of cHAp, respectively. The empirical evidence of the presence of the ν_3(O-Se-O) vibration in the spectrum of Se-HAp in the 660 – 830 cm^{-1} range indicates that selenite was introduced successfully into the unit cell of HAp and is a good match with the theoretical predictions. Based on the calculated band positions, the covering of the broad range of wavenumber values by this vibration in the experimentally measured spectrum of Se-HAp (Fig.6a) cannot

unequivocally indicate one or the other type of cHAp substitution, but most probably points at a mixture thereof, *i.e.* AB-type.

Fig.11 illustrates the temperature dependence of different thermodynamic parameters, including entropy (S), enthalpy (H), heat capacity (C_p) and the Gibbs free energy (G) in different types of cHAp before and after the incorporation of selenite. Entropy increases exponentially with temperature, indicating the increasing structural disorder and randomness of states owing to the deterioration of cHAp crystallinity accompanying the incorporation of the selenite ion. Even though there was no difference in the entropy of various cHAp types before and after the addition of selenite in the lowest temperature range, i.e. up to 100 °C, the difference became obvious at higher temperatures, reaching the maximum at 1000 °C. The entropy of different cHAp types adopted the following trend: AB > A > B. Concerning C_p, it rapidly increased up to 500 °C, when it started to wind down, reaching saturation by 1000 °C. In the first stage, it shows the same trend as entropy, which means equal values for the antagonistic types (before and after the substitution), but after 500 °C selenite-doped AB-HAp took on the highest value and maintained it throughout the entire remaining temperature range. Enthalpy underwent an exponential growth as the function of temperature and also displayed a distinct difference between the different types of cHAp, adopting the following trend: AB > B >A. This order refers to the internal stability at the chemical bond level and matches the aforementioned predictions regarding the stability of different types of selenite-substituted cHAp. In addition, the enthalpy of all types of cHAp was higher before the introduction of selenite than after it. A system with the least number of crystalline defects appears to be the most energetically favored, exhibiting the highest enthalpy values. This trend may be explained by the fact that AB-type cHAp accommodating selenite is unique in a sense that it maintains the number of Ca^{2+} ions in the unit cell at 10. B-type cHAp does not preserve this total number of Ca^{2+} ions, but it preserves its hydroxyl group, the reason for which it comes right after AB-type in the order of stability with respect to enthalpy. The lowest enthalpy is ascribed to selenite-doped A-type cHAp because it does not only lose one Ca^{2+} ion per substitution, but it also loses its hydroxyl group. Finally, as expected from the relationship between ΔH and ΔS in deriving the free energy term, i.e. $\Delta G = \Delta H - T\Delta S$, the Gibbs free energy exponentially decreased with temperature up to 1000 °C. It followed the same trend as enthalpy and the negative values of ΔG as a function of temperature indicate the tendency of the crystal for stability.

Overall, these simulations corroborated the empirical findings regarding the effects that selenite exerts on the crystalline order in HAp. In addition, they indicated that the most energetically favored crystal structure is that belonging to AB-type cHAp, followed by the B-type and only then by the A-type. This order of stability was entailed by the variation in the geometry and orientation of the selenite ion. The preferred substitution site for selenite in A-type cHAp is phosphate and in the B- and AB-types it is carbonate. The lattice parameters a, b, α, β and Ω decreased significantly, while the parameters c and γ increased slightly upon the introduction of selenite to A-type cHAp. The effect was different in B-type cHAp, where all lattice parameters increased except β, which decreased considerably. In AB-type cHAp, all unit cell dimensions decreased and the opposite effect applied to the unit cell angles. Combined with the empirical data, which showed that both as-precipitated Se-HAp and annealed Se-HAp at higher selenite concentrations display simultaneously decreased

lattice parameters *a* and *c*, these results suggest that the AB-type model of substitution in cHAp may indeed best describe the structural effects caused by the introduction of selenite into HAp. The empirically evidenced expansion of the lattice at very low selenite concentrations may suggest that even though substitution of phosphates is less thermodynamically favorable, it may still occur due to kinetic reasons during chemical precipitation under ambient conditions, when the concentration of defects becomes considerable and crystallinity drops dramatically. In this case the B-type model is suitable for the description of the structural accommodation of the selenite ion. As far as the A-type is concerned, not only was its substitution not matched with the empirical results, but it also presents a form of cHAp that is the least energetically favorable and the least probable as such. To conclude, as suggested by both empirical and theoretical findings, carbonate, not phosphate presents the most probable ion that selenite replaces upon entering the crystal structure of HAp. This coupling of the experimental approaches with quantum mechanical modeling could provide a helpful way to develop a deeper understanding of HAp doped with different elements as agents for various medical applications.

3.3. Biological response analysis

Remarkable biosafety profile is one of the hallmarks of HAp nanoparticles. Having entered the cell, say to deliver a nucleic acid[85], polypeptide[86] or small-molecule[87] cargo, these nanoparticles *per se* normally do not cause any toxic effects, the reason being their relatively slow dissolution even in the most acidic milieu of the late lysosome, allowing the Ca^{2+} pumps on the plasma and mitochondrial membranes sufficient time to lower the temporarily increased cytosolic calcium concentration down to normal levels[88]. However, for certain therapeutic applications, moderate to high toxicity is desired, as, for example, upon penetrating certain biological barriers or targeting pathogenic cells, be they bacterial or malign, or healthy cells whose metabolism is in need of downregulation, such as overactive bone-lysing osteoclasts. In those cases, increased solubility of HAp and a higher release rate of chemotherapeutic loads or potentially toxic Ca^{2+} and other ions is desirable. Lattice deformations induced by the addition of the carbonate specie, a substitute analogous to selenite given its divalent anionic nature and BO_3 stoichiometry, for example, result in increased solubility[89]. To test the effect of $PO_4^{3-} \rightarrow SeO_3^{2-}$ substitution on solubility of HAp, Ca^{2+} release measurements were performed and the results are shown in Fig.12a. At 11.4 mg/l, the measured solubility of pure HAp was by about an order of magnitude higher than the theoretical value obtained for sintered HAp[90]. This higher value is explained by the mildly acidic, osteoclast-mimicking conditions used (pH 6.8 at 25 °C), but also by the higher concentration of crystallographic defects and the dissolution of poorly crystalline domains on the particle surface, naturally present in as-precipitated powders. Solubility value for Se-HAp accommodating 1.2 wt.% of selenite was 2.5 times higher than that for undoped HAp; at 25 mg/l, it was higher than for calcite (13 mg/l), but lower than for brushite and monetite (both ~ 48 mg/l)[91] (Fig.12b). At 2.2 after 24 h of the immersion time, the solubility ratio between Se-HAp and HAp was lower than the ratio between the solubilities of amorphous CP and HAp (~ 2.7 x), but higher than the ratio between sintered whitlockite (β-TCP) and HAp (~ 1.7 x). Whitlockite is the phase combined with HAp in biphasic bone cements to increase the resorbability of the latter and provide a better match with the new bone ingrowth rate. Se-HAp as a HAp compound that combines the higher resorbability of β-TCP

and osteoconductivity provided by the HAp composition could thus have the same positive effect on bone regeneration as β-TCP/HAp biphasic bone replacement materials do. The ideal solubility profile is achieved already at 1.2 wt.% of selenite, the range at which the pockets of order and disorder in the material are still balanced, unlike at higher concentrations, when the structure-breaking propensity of the selenite ion gets more pronounced. Mechanistically, the increased solubility of Se-HAp compared to HAp is explainable by the fact that even though the two oxyanions involved in $PO_4^{3-} \rightarrow SeO_3^{2-}$ substitution are similar in size, the substitution is not isoelectric in nature. The aforementioned charge balance reasons (Fig.1) lead to the "opening" of the crystal structure in the sense of increasing the concentration of vacancies and lattice voids in it and broadening the distribution of bond lengths and angles, thus effectively lowering the crystalline order and making the overall structure less stable and more soluble.

Achieving a precise balance between the activity of mutually antagonistic osteoblasts and osteoclasts in the region of bone in contact with the implant is required for the seamless implant integration process to occur. Given that the usually mild foreign body response and inflammation accompanying the first stages in wound healing following the implantation recruit osteoclasts and other phagocytic cells that may prematurely resorb the material[92,93], it is of crucial importance to ensure that the implants stimulate the osteoblastic, bone-building activity and slow down the osteoclastic, bone-lysing activity. In our previous study we demonstrated that Se-HAp exhibits an osteoinductive effect on osteoblastic cells[25] and here we complement these analyses by assessing the comparative effect of Se-HAp against osteoblastic and osteoclastic cells. To that end, we first administered Se-HAp powders and RANKL, the differentiation agent, simultaneously to undifferentiated RAW264.7 cells and measured the cell viability after different periods of time. The osteoclastic cells uptake Se-HAp nanoparticles and undergo differentiation accompanied by the formation of polynuclear cells shown in Fig.13. As seen in Fig.14a, more than 10x lower concentration of selenite than that which produced a desirable solubility profile in Se-HAp (1.2 wt.%) was sufficient to produce a therapeutically advantageous effect of suppressed RAW264.7 osteoclast activity at concentrations equal to or higher than 2.5 mg/ml. While selenite contents higher than 1.9 wt.% reduced the osteoclast viability even at the lowest tested concentration of 1 mg/ml (data not shown), Se-HAp powders containing 0.1 and 1.2 wt.% of selenite inhibited osteoclasts only at concentrations higher than or equal to 2.5 mg/ml (Fig.14a). The viability reduction effect was both particle-dose-dependent and selenite-concentration-dependent, as seen by the progressive decrease in viability following an increase in the concentration of the powders that the cells were exposed to and an increase in the concentration of selenite in Se-HAp from 0.1 to 1.2 wt.%, respectively. Thus, while neither 0.1 or 1.2 wt.% Se-HAp powders affected the viability at 1 mg/ml, they reduced the viable cell population by ~ 50 % at 2.5 mg/ml and down to ~ 15 – 20 % at 5 mg/ml (Fig.14a).

At the same time, the viability of cells challenged with any given amount of the powder dropped in direct proportion with the selenite content in it. As shown in Fig.14b, the cell viability decreased as the amount of selenite captured inside the particles increased, demonstrating that the osteoclast inhibition is due to the release of the selenite ion. Since this ion can be assumed to be distributed evenly through the structure of Se-HAp particles as the result of co-precipitation, the release of selenite during dissolution can be expected to

follow the release of calcium ions. Some level of incongruent dissolution may occur, but it must be finite considering the ionic nature of HAp crystals and a limited capacity with which the charge imbalance due to a selective release of a single type of ion can be sustained. Therefore, based on the solubility data (Fig.12), the concentration of released selenite from 1.2 wt.% Se-HAp at the lowest tested concentration of 1 mg/ml could be estimated at 300 ng/ml (i.e., 2.36 μM) and at this level no diminishment of the viable and metabolically active osteoclast population was observed (Fig.14a). Most interestingly, the analysis of a comparative effect of Se-HAp on two osteoblastic cell lines, K7M2 and MC3T3-E1, and osteoclastic RAW264.7 cells demonstrated a considerably greater reduction in the viability of osteoclastic cells than of their osteoblastic counterparts when both are treated with identical amounts of Se-HAp particles. Thus, as seen in Fig.15, while the viabilities of K7M2 and MC3T3-E1 challenged with 5 mg/ml Se-HAp containing either 0.1 or 1.2 wt.% selenite exceeded 60 % relative to the negative control, the viabilities of RAW264.7 were significantly lower at 21.2 and 15.4 %, respectively. Meanwhile, no similar osteoblast vs. osteoclast selectivity was detected for Se-free HAp, for which the viabilities of K7M2 osteoblasts and RAW264.7 osteoclasts exceeded 100 % relative to the negative control and the viability of osteoblastic MC3T3-E1 cells equaled 83.9 % (Fig.15). This has indicated that this therapeutically promising selective effect is due to selenite ions delivered by HAp rather than to HAp alone.

The inhibitory effect of selenite delivered beyond the threshold delineable from Fig.14b is obvious and expected considering that *in vitro* exposure of PLHC-1 hepatoma cells to selenite concentrations higher than 10 mM for 24 h induced mitochondrial membrane damage, DNA deterioration, increased generation of reactive oxygen species and caspase-3 upregulation, resulting in apoptotic and necrotic mediated cell death[94]. A number of *in vivo* studies corroborate this dose-dependency of the effects on selenium species on biological systems. Selenium and its oxides administered to mice in doses of up to 40 μg/kg body weight exerted an array of beneficial effects, including reduced cancer risk and improved thyroid function, but caused intense oxidative stress and injury to liver and kidneys at higher concentrations[95]. Administered intramuscularly to sheep, sodium selenite produced edematous lungs and pale mottled hearts in animals and its lethal dose, LD50, was only 0.7 mg/kg body weight[96]. Likewise, in Japanese rice fish, pericardial edema and craniofacial disfigurements were some of the malformations detected in the offspring of the population treated through diet with selenite ions, the toxicity of which exceeded that of selenium nanoparticles[97]. The effects of selenium species are also intensely dependent on the oxidation state and the chemical form - anionic, organometallic, elemental – in which selenium is delivered, in such a way that, for example, the average oral LD_{50} for sodium selenite in rats was almost 1000 times lower than that for elemental selenium (7 vs. 6700 mg/kg body weight)[98,99].

All in all, numerous studies on the effects of selenium and its compounds on mammalian species resulted in the conclusion that the window between deficiency and toxicity of selenium is very narrow[100]. Optimizing the content of selenite in HAp is thus necessary in order to reach the thin line where stress induced to the cell and/or the tissue by the foreign specie is such that it has a positive, hormetic effect. Such effects abound in the literature, including the enhancement of the effectiveness of gene therapy when inflammatory

pathways are made active[101]; the boost of the cell immunity being paralleled by an increase in intracellular superoxide production[102] and the negative effect of the quenching of H_2O_2 on a number of essential signaling pathways inside the cell[103], including those governing glucose metabolism[104]; the greater ability of hypoxic mesenchymal stem cells to pass across the blood brain barrier[105]; and the greater osteogenic potential of osteoblasts subjected to moderate mechanochemical stress[106]. Nevertheless, with the tolerable upper intake level of selenite being estimated at ~ 1 mg/kg body weight[107], it would take the resorption of more than 5 g of 1.2 wt.% Se-HAp to exceed these safety levels in an averagely sized human (62 kg). The realistic nature of this scenario necessitates detailed in vivo safety studies before Se-HAp reported here can be used clinically in bone grafts for tissue engineering.

Conclusions

Selenite is a prospective dopant in HAp, capable of endowing it with a multifunctional response utilizable for a variety of therapeutic or prophylactic applications. We previously deduced a triad of properties that the selenite ion induces or potentiates in HAp: antibacterial, osteoinductive and anticancer[25]. In this follow-up study we synthesized a series of selenite-doped HAp nanopowders and analyzed them from a threefold perspective: (1) physicochemical characterization; (2) density functional theory; and (3) biological response analysis. Structural characterization using diffractometric, spectroscopic and microstructural techniques has demonstrated that selenite lowers the crystallinity of doped HAp. Albeit a structure breaker, however, it brings about increased order at local and global scales within specific concentration windows. Quantum mechanical modeling of the accommodation of selenite in the three different types of carbonated HAp resulted in minimum energy states for substitution in each system, from which preferred crystal symmetries were deduced. Complementing the physicochemical characterization, which provided insights into the global structural effects of the integration of selenite, *ab initio* simulations described local effects, at the level of a single unit cell of Se-HAp. Infrared bands were computed and confirmed the successful trapping of selenite in the structure of carbonated HAp. The internal stability of AB-type carbonated HAp accommodating selenite was higher than that of the B-type and, particularly, the A-type.

As far as the biological activity is concerned, doping with the selenite ion allowed HAp to complement its osteoinductive nature with the ability to inhibit the osteoclastic activity. The effect was highly selective, enabling Se-HAp to diminish the viability of osteoclasts to a significantly higher degree than that of their osteoblastic counterparts. As with all *in vitro* assaying, however, caution must be exercised or else premature and overly generalized conclusions could be drawn. For example, in the case of HAp for gene delivery, transfection in planar cell cultures is more efficient when agglomerated particles are used[85], capable of capturing larger amounts of the genetic material and penetrating the plasma membrane more effectively, even though one such system may lead to embolism and/or rapidly react with the negatively charged epithelial cells long before it reaches its endothelial target *in vivo*. Aside from implicitly insinuating that the future belongs to experimental models that would lie between the über-simplicity of planar cell culture and the black box complexity of whole organism *in vivo* models, this lateral thought evokes the concern that a similar disparity between *in vitro* optimizations and *in vivo* potential might be immanent in this case too.

Thus, there is always a finite possibility that the inhibitory effects detected under *in vitro* conditions will be diluted and neutralized under *in vivo* conditions, when the interaction between the agent and the target is engrossed by a more complex physical context.

Another aspect where uncertainties must be humbly accepted with respect to the results of this study stems from the multivariable nature of all physical systems. As usual, the effects of a single modification in a material are such that they produce more than one substantial change to it. The addition of selenite has thus not only added a new ionic entity to HAp, but it also affected the crystallinity, the lattice strain, the particle size and morphology and other microstructural parameters. Each of these variations synergizes with others and their total effect on the response of the material in a biological setting may be difficult to predict or control. Isotropic amorphization of HAp due to incorporation of selenite, for example, can have dual effects on osteoporotic and normal bone. One possibility is that the selenite-enriched bone mineral, as demonstrated in this study, would release selenite ions into the extracellular matrix and thereby hinder the osteoclastic resorption. The opposite effect, however, is equally possible, involving the shift of the material toward a more resorbable state as per La Chatelier's principle and as per the law dictating the inverse proportionality between crystallinity and solubility. However, since amorphous calcium phosphate is a precursor for the mineralization of biogenic apatite and also a natural transient phase *en route* to its resorption[108], the amorphization effect achieved by doping with selenite could have an accelerating effect on bone regeneration and not necessarily improve resorption, as it could be intuitively assumed in analogy with the higher absorption rate of amorphous oral pharmaceutical formulations. One way of figuring out which of these two effects is the key determinant of the fate of the regenerated bone is to resort to *in vivo* tests. Hastily turning to *in vivo* studies, however, often comes at the expense of fundamental insights into the material/tissue interaction. Another way of answering this question takes us to more detailed and rigorous insights at the finest scales investigable using state-of-the-art physicochemical techniques and/or more imaginative classical approaches. Which of these two routes will be taken falls largely within the realm of the personal preference of the investigator, but also the current trends in the field. Hope remains that these trends will not carry us blindly into the reigns of drained creativity and that approaches could be thought of that do not follow the vogue, but rather defy and challenge it.

Supplementary Material

Refer to Web version on PubMed Central for supplementary material.

Acknowledgements

The United States NIH/NIDCR grant R00-DE021416 is acknowledged for support. S. Tang from the Uskoković Lab is thanked for technical assistance with the synthesis of Se-HAp powders and FTIR measurements. M. A. Iyer from the Uskoković Lab is thanked for technical assistance with the XRD measurements. T. Aoki from the Materials Research Institute at University of California in Irvine is thanked for technical assistance with HR-TEM.

References

1. Uskoković V, The Role of Hydroxyl Channel in Defining Selected Physicochemical Peculiarities Exhibited by Hydroxyapatite, RSC Adv. 5 (2015) 36614–36633. [PubMed: 26229593]

2. Uskoković V, Ion-Doped Hydroxyapatite: An Impasse or the Road to Follow?, Ceram. Int. 46 (2020) 11443–11465.

3. Mayer I, Berger U, Markitziu A, Gedalia I, The uptake of lithium ions by synthetic carbonated hydroxyapatite, Calcif. Tissue Int. 38 (1986) 293–295. [PubMed: 3087603]

4. Arslan A, Cakmak S, Gumusderelioglu M, Enhanced osteogenic activity with boron-doped nanohydroxyapatite-loaded poly(butylene adipate-co-terephthalate) fibrous 3D matrix. Artificial Cells, Nanomedicine, and Biotechnology 46 (2018) 790–799.

5. Ciobanu G, Bargan AM, Luca C, New Bismuth-Substituted Hydroxyapatite Nanoparticles for Bone Tissue Engineering. JOM 67 (2015) 2534–42.

6. Chatelain G, Bourgeois D, Ravaux J, Averseng O Vidaud C, Meyer D, Incorporation of uranium into a biomimetic apatite: physicochemical and biological aspects. J. Biol. Inorg. Chem. 20 (2015) 497–507. [PubMed: 25534663]

7. Vance ER, Zhang Y, McLeod T, Jovanovic M. Preparation of Pu-doped fluoroapatite. Journal of Nuclear Materials 426, 223–5 (2012).

8. Ignjatović NL, Mančić L, Vuković M, Stojanović Z, Nikolić MG, Škapin S, Jovanović S, Veselinović Lj., Uskoković V, Lazić S, Marković S, Lazarević M, Uskoković DP – "Rare-Earth (Gd3+, Yb3+/Tm3+, Eu3+) Co-Doped Hydroxyapatite as Magnetic, Up-Conversion and Down-Conversion Materials for Multimodal Imaging", Scientific Reports 9, 16305 (2019). [PubMed: 31705047]

9. Prosolov KA, Belyavskaya OA, Linders J, Loza K, Prymak O, Mayer C, Rau JV, Epple M, Sharkeev YP. Glancing Angle Deposition of Zn-Doped Calcium Phosphate Coatings by RF Magnetron Sputtering. Coatings, 9, 220–236 (2019).

10. Sedelnikova MB, Komarova EG, Sharkeev YP, Ugodchikova AV, Tolkacheva TV, Rau JV, Buyko EE, Ivanov VV, Sheikin VV. Modification of titanium surface via Ag-, Sr- and Si-containing micro-arc calcium phosphate coating. Bioactive Materials 4, 224–235 (2019). [PubMed: 31406950]

11. Filankembo A, Giorgio S, Lisiecki I, Pileni MP, Is the Anion the Major Parameter in the Shape Control of Nanocrystals, Journal of Physical Chemistry B 107 (30), 7492–7500 (2003).

12. Kunz W, Specific Ion Effects in Colloidal and Biological Systems, Current Opinion in Colloid & Interface Science 15, 34–39 (2010).

13. Amenta E, King HE, Petermann H, Uskoković V, Tommasini SM, Macica CM, Vibrational Spectroscopic Analysis of Hydroxyapatite in HYP Mice and Individuals with XLH, Therapeutic Advances in Chronic Disease 9 (12) 268–281 (2018). [PubMed: 30719271]

14. Rodriguez-Valencia C, Lopez-Alvarez M, Cochon-Cores B, Pereiro I, Serra J, Gonzalez P, Novel selenium-doped hydroxyapatite coatings for biomedical applications. Journal of Biomedical Materials Research A 101:853–61 (2013).

15. Rayman MP – "Selenium and human health", Lancet 379, 1256–1268 (2012). [PubMed: 22381456]

16. Roman M, Jitaru P, Barbante C – "Selenium biochemistry and its role for human health", Metall 6, 25–54 (2014).

17. Chen J, Berry MJ – "Selenium and selenoproteins in the brain and brain diseases", J. Neurochem. 86, 1–12 (2003). [PubMed: 12807419]

18. Qingqing H, Yiyun L, Xu Q, Lijie Z, Xuefeng L, Yingming X – "Selenite mitigates cadmium-induced oxidative stress and affects Cd uptake in rice seedlings under different water management systems", Ecotoxicol. Environ. Saf. 168, 486–494 (2018). [PubMed: 30423513]

19. Yang YW, Liou SH, Hsueh YM, Lyu WS, Liu CS, Liu HJ, Chung MC, Hung PH, Chung CJ – "Risk of Alzheimer's disease with metal concentrations in whole blood and urine: A case-control study using propensity score matching", Toxicol. Appl. Pharmacol. 356, 8–14 (2018). [PubMed: 30025849]

20. Deyab G, Hokstad I, Aaseth J, Smastuen MC, Whist JE, Agewall S, Lyberg T, Tveiten D, Hjeltnes G, Zibara K, Hollan I – "Effect of anti-rheumatic treatment on selenium levels in inflammatory arthritis", J. Trace Elem. Med. Biol. 49, 91–97 (2018). [PubMed: 29895378]

21. Močenić I, Kolić I, Nišević JR, Belančić A, Tratnik JS, Mazej D, Falnoga I, Vlašić-Cicvarić I, Štimac T, Špirić Z, Horvat M, Prpić I – "Prenatal selenium status, neonatal cerebellum measures

and child neurodevelopment at the age of 18 months", Environmental Research 176, 108529 (2019). [PubMed: 31255949]

22. Schrauzer GN, Meginness JE – "Observations on human selenium supplementation", Trace Substances and Environmental Health 13, 64–82 (1978).
23. Chu J-Z, Yao X-Q, Si C, Liu G-X, Ma C-H – "Responses of physiological traits and nutritional ingredients content in flowers of medicinal chrysanthemum to selenium application at different growth stages", Journal of Food and Nutrition Research 2, 575–581 (2014).
24. Đokić V, Glushkova A, Andričević P, Arakcheva A, Kollar M, Horvath E, Forro L. Photovoltaic perovskites for high sensitive X-ray detection. In: Programme and the Book of Abstracts, Twenty-First Annual Conference YUCOMAT 2019 & Eleventh World Round Table Conferences on Sintering WRTCS 2019, edited by Uskoković DP and Radmilović VR, Materials Research Society of Serbia, Belgrade (2019), pp. 50.
25. Uskoković V, Iyer MA, Wu VM – "One Ion to Rule Them All: Combined Antibacterial, Osteoinductive and Anticancer Properties of Selenite-Incorporated Hydroxyapatite", Journal of Materials Chemistry B 2017, 5, 1430–1445 (2017). [PubMed: 28944060]
26. Moreno-Reyes R, Egrise D, Neve J, Pasteels JL, and Schoutens A, "Selenium deficiency-induced growth retardation is associated with an impaired bone metabolism and osteopenia.," J. Bone Miner. Res. 16, 1556–1563 (2001). [PubMed: 11499879]
27. Cao JJ, Gregoire BR, Zeng H – "Selenium deficiency decreases antioxidative capacity and is detrimental to bone microarchitecture in mice", J. Nutr. 142, 1526–1531 (2012). [PubMed: 22739365]
28. Turan B, Can B, Delilbasi E – "Selenium combined with vitamin E and vitamin C restores structural alterations of bones in heparin-induced osteoporosis", Clin Rheumatol 22, 432–436 (2003). [PubMed: 14677021]
29. Vekariya KK, Kaur J, Tikoo L – "Alleviating anastrazole induced bone toxicity by selenium nanoparticles in SD rats", Toxicol Appl Pharmacol 268, 212–220 (2013). [PubMed: 23415680]
30. Uskoković V, Desai TA – "Phase Composition Control of Calcium Phosphate Nanoparticles for Tunable Drug Delivery Kinetics and Treatment of Osteomyelitis. II. Antibacterial and Osteoblastic Response", Journal of Biomedical Materials Research Part A 101 (5) 1427–1436 (2013). [PubMed: 23115128]
31. Uskoković V, Janković-Častvan I, Wu VM – "Bone Mineral Crystallinity Governs the Orchestration of Ossification and Resorption during Bone Remodeling", ACS Biomaterials Science and Engineering 5, 3483–3498 (2019).
32. Chan CK, Mason A, Cooper C, Dennison E – "Novel advances in the treatment of osteoporosis", British Medical Bulletin 119, 129–42 (2016). [PubMed: 27558130]
33. Sözen T, Özışık L, Başaran NÇ, An overview and management of osteoporosis, Eur J Rheumatol. 4(1):46–56 (2017). [PubMed: 28293453]
34. Reid IE, Bolland MJ, Grey A – "Effects of vitamin D supplements on bone mineral density: a systematic review and meta-analysis", Lancet 383, 146–55 (2014). [PubMed: 24119980]
35. Khan M, Cheung AM, Khan AA – "Drug-Related Adverse Events of Osteoporosis Therapy", Endocrinol Metab Clin North Am. 46, 181–192 (2017). [PubMed: 28131131]
36. Augustine M, Horwitz MJ – "Parathyroid hormone and parathyroid hormone-related protein analogs as therapies for osteoporosis", Curr. Osteoporosis Rep. 11, 400–6 (2013).
37. Yao W, Dai W, Jiang L, Lay EY, Zhong Z, Ritchie RO, Li X, Ke H, Lane NE – "Sclerostin-antibody treatment of glucocorticoid-induced osteoporosis maintained bone mass and strength", Osteoporosis Int. 27, 283–294 (2016).
38. Fessio A, Rossini M, Viapiana O, Idolazzi L, Benini C, Vantaggiato E, Gatti D – "New strategies for the prevention and treatment of systemic and local bone loss; from pathophysiology to clinical application", Curr. Pharm. Des. 23, 6241–6250 (2017). [PubMed: 28707576]
39. Mittemeijer EJ, Wetzel U – "The "state of the art" of the diffraction analysis of crystallite size and lattice strain", Zeitschrift für Kristallographie 223, 552–560 (2008).
40. Albetran H, Vega V, Prida VM, Low IM. Dynamic Diffraction Studies on the Crystallization, Phase Transformation, and Activation Energies in Anodized Titania Nanotubes. Nanomaterials (Basel). 2018 2; 8(2): 122.

41. Faust JJ, Christenson W, Doudrick K, Ros R, Ugarova TP, Development of fusogenic glass surfaces that impart spatiotemporal control over macrophage fusion: Direct visualization of multinucleated giant cell formation. Biomaterials 2017;128:160–71. [PubMed: 28340410]
42. Yao F, LeGeros J, LeGeros RZ – "Simultaneous Incorporation of Carbonate and Fluoride in Synthetic Apatites: Effect on Crystallographic and Physico-Chemical Properties", Acta Biomaterialia 5, 2169–2184 (2009). [PubMed: 19269268]
43. LeGeros RZ – "Calcium Phosphate-Based Osteoinductive Materials", Chemical Society Reviews 108 (11) 4742–4753 (2008).
44. Suetsugu Y, Takanashi Y, Okamura FP, Tanaka J – "Structure Analysis of A-Type Carbonate Apatite by a Single-Crystal X-Ray Diffraction Method", Journal of Solid State Chemistry 155, 292–304 (2000).
45. Kaflak A, Moskalewski S, Kolodziejski W – "The solid-state proton NMR study of bone using a dipolar filter: apatite hydroxyl content versus animal age", RSC Advances 9, 16909–16918 (2019).
46. Taylor AJ, Rendina E, Smith BJ and Zhou DH, Analyses of mineral specific surface area and hydroxyl substitution for intact bone, Chem. Phys. Lett, 2013, 588, 124–130.
47. Eanes ED, Termine JD, Nylen MU – "An electron microscopic study of the formation of amorphous calcium phosphate and its transformation to crystalline apatite", Calcif. Tiss. Res. 12, 143–158 (1973).
48. Barton SS, Harrison BH – "Surface and bulk properties of amorphous calcium phosphate", In: Kerker M (ed.), Colloid and Interface Science Vol. 3, Academic Press, New York, NY, pp. 71 (1976).
49. Pentsak EO, Eremin DB, Gordeev EG, Ananikov VP – "Phantom reactivity in organic and catalytic reactions as a consequence of microscale destruction and contamination-trapping effects of magnetic stir bars", ACS Catal. 9, 3070–3081 (2019).
50. Chikarakara E, Fitzpatrick P, Moore E, Levingstone T, Grehan L, Higginbotham C, Vázquez M, Bagga K, Naher S, Brabazon D, In vitro fibroblast and pre-osteoblastic cellular responses on laser surface modified Ti-6Al-4V, Biomed Mater 10(1):015007 (2014). [PubMed: 25546881]
51. Vilardell AM, Cinca N, Garcia-Giralt N, Dosta S, Cano IG, Nogués X, Guilemany JM, Osteoblastic cell response on high-rough titanium coatings by cold spray, J Mater Sci Mater Med. 29(3):19 (2018). [PubMed: 29392501]
52. Brinkmann J, Hefti T, Schlottig F, Spencer ND, Hall H, Response of osteoclasts to titanium surfaces with increasing surface roughness: an in vitro study, Biointerphases 7(1–4):34 (2012). [PubMed: 22639093]
53. Müller B, Tailoring biocompatibility: Benefitting patients. Materials today 2010;13:58.
54. Tang MT, Ulissi ZW, Chan K. Theoretical Investigations of Transition Metal Surface Energies under Lattice Strain and CO Environment. J. Phys. Chem. C 2018, 122, 26, 14481–14487
55. Uskoković V, Li W, Habelitz S – "Amelogenin as a Promoter of Nucleation and Crystal Growth of Apatite", Journal of Crystal Growth 316, 106–117 (2011). [PubMed: 30828107]
56. Uskoković V - "Disordering the Disorder as the Route to a Higher Order: Incoherent Crystallization of Calcium Phosphate through Amorphous Precursors", Crystal Growth and Design 19 (8) 4340–4357 (2019).
57. LeGeros RZ, Apatites in biological systems. Prog Crystal Growth Charact. 4:1–45 (1981).
58. Henneman ZJ, Nancollas GH, Ebetino FH, Russell RGG, Phipps RJ – "Bisphosphonate binding affinity as assessed by inhibition of carbonated apatite dissolution in vitro", J Biomed Mater Res A. 85(4): 993–1000 (2008). [PubMed: 17907244]
59. Kolmas J, Oledzka E, Sobczak M, Nalecz-Jawecki G, Nanocrystalline hydroxyapatite doped with selenium oxyanions: a new material for potential biomedical applications. Materials Science & Engineering C 2014;39:134–42. [PubMed: 24863209]
60. Sun J, Zheng X, Li H, Fan D, Song Z, Ma H, Hua A, Hui J, Monodisperse selenium-substituted hydroxyapatite: Controllable synthesis and biocompatibility. Materials Science & Engineering C 2017;73:596–602. [PubMed: 28183650]
61. Monteil-Rivera F, Fedoroff M, Jeanjean J, Minel L, Barthes MG, Dumonceau J, Sorption of Selenite (SeO(3)(2-)) on Hydroxyapatite: An Exchange Process. Journal of Colloid and Interface science 2000;221:291–300. [PubMed: 10631033]

62. Yanhua W, Hao H, Li Y, Zhang S, Selenium-substituted hydroxyapatite nanoparticles and their in vivo antitumor effect on hepatocellular carcinoma. Colloids and Surfaces B 2016;140:297–306
63. Weidenthaler C – "Pitfalls in the characterization of nanoporous and nanosized materials", Nanoscale 3, 792–810 (2011). [PubMed: 21229179]
64. Linnikov OD – "Relations between Activation Energies for Nucleation and of Growth of Crystals", Nanosystems: Phys. Chem. Math. 4, 546–552 (2014).
65. Pacurariu C, Lazau RI, Lazau I, Ianos R, Vlase T, Influence of the specific surface area on crystallization process kinetics of some silica gels. J. Thermal Analysis and Calorimetry 97, 409 (2009).
66. Gramain P, Schaad P – "Dissolution of Calcium Hydroxyapatite", In: Interfacial Dynamics, edited by Nikola Kallay, Marcel Dekker, New York (2000), pp. 492.
67. Pratapa S, O'Connor B – "Development of MgO ceramic standards for X-ray and neutron line broadening assessments", JCPDS-International Centre for Diffraction Data 2002, Advances in X-Ray Analysis, Volume 45, pp. 41–48 (2002).
68. Ma J, Wang Y, Zhou L, Zhang S, Preparation and characterization of selenite substituted hydroxyapatite, Mater Sci Eng C Mater Biol Appl. 1;33(1):440–5(2013). [PubMed: 25428093]
69. Hughes JM, Rakovan JF – "Structurally robust chemically diverse: apatite and apatite supergroup minerals" Elements 11, 165–170 (2015).
70. Penel G, Leroy G, Rey C, Bres E – "Micro Raman Spectral Study of the PO_4 and CO_3 Vibrational Modes in Synthetic and Biological Apatites", Calcified Tissue International 63, 475–481 (1998). [PubMed: 9817941]
71. Wang Y, Ma J, Zhou L, Chen J, Liu Y, Qiu Z, Zhang S, Dual functional selenium-substituted hydroxyapatite. Interface Focus 2012;2:378–86. [PubMed: 23741613]
72. Layani JD, Cuisinier FJ, Steuer P, Cohen H, Voegel JC, Mayer I – "High-resolution electron microscopy study of synthetic carbonate and aluminum containing apatites", J. Biomed. Mater. Res. 50, 199–207 (2000). [PubMed: 10679685]
73. Marković S, Veselinović Lj., Lukić M, Karanović Lj., Bračko I, Ignjatović N, Uskoković D – "Synthetical bone-like and biological hydroxyapatites: a comparative study of crystal structure and morphology", Biomedical Materials 6 (2011) 045005. [PubMed: 21659698]
74. Barralet JE, Best SM, Bonfield W – "Effect of sintering parameters on the density and microstructure of carbonate hydroxyapatite", J. Mater. Sci. Mater. Med. 11, 719–24 (2000). [PubMed: 15348078]
75. Tonegawa T, Ikoma T, Yoshioka T, Hanagata N, Tanaka J – "Crystal Structure Refinement of A-Type Carbonate Apatite by X-Ray Powder Diffraction", Journal of Materials Science 45, 2419–2426 (2010).
76. Fleet ME, Lui X, King P – "Accommodation of the Carbonate Ion in Apatite: An FTIR and X-Ray Structure Study of Crystals Synthesized at 2–4 GPa", American Mineralogy 89, 1422–1434 (2004).
77. Yoruc ABH, Aydinoglu A, The precursors effects on biomimetic hydroxyapatite ceramic powders. Materials Science & Engineering C 2017;75:934–46. [PubMed: 28415549]
78. Mansour SF, El-Dek SI, Ahmed MK, Physico-mechanical and morphological features of zirconia substituted hydroxyapatite nano crystals. Scientific Reports 2017;7:43202. [PubMed: 28256557]
79. Šupová M, Substituted hydroxyapatites for biomedical applications: A review. Ceramics International 2015;41:9203–31.
80. Zhao Z, Espanol M, Guillem-Marti J, Kempf D, Diez-Escudero A, Ginebr MP, Ion-doping as a strategy to modulate hydroxyapatite nanoparticle internalization. Nanoscale 2016;8:1595–607. [PubMed: 26690499]
81. Zilm ME, Chen L, Sharma V, McDannald A, Jain M, Ramprasad R, Wei M, Hydroxyapatite substituted by transition metals: experiment and theory. Physical Chemistry Chemical Physics 2016;18:16457–65. [PubMed: 27264723]
82. Youness RA, Taha MA, Elhaes H, Ibrahim M, Molecular modeling FTIR spectral characterization and mechanical properties of carbonated-hydroxyapatite prepared by mechanochemical synthesis. Materials Chemistry and Physics 2017;190:209–18.

83. Zuo G, Wei X, Sun H, Liu S, Zong P, Zeng X, Shen Y, Morphology controlled synthesis of nano-hydroxyapatite using polyethylene glycol as a template. Journal of Alloys and Compounds 2017;692:693–7.
84. Ren F, Lu X, Leng Y, Ab initio simulation on the crystal structure and elastic properties of carbonated apatite. Journal of the mechanical behavior of biomedical materials 2013;26:59–67. [PubMed: 23811277]
85. Khan MA, Wu VM, Ghosh S, Uskoković V – "Gene Delivery Using Calcium Phosphate Nanoparticles: Optimization of the Transfection Process and the Effects of Citrate and Poly(L-Lysine) as Additives", Journal of Colloid and Interface Science 471, 48–58 (2016). [PubMed: 26971068]
86. Uskoković V, Ghosh S, Wu VM – "Antimicrobial Hydroxyapatite-Gelatin-Silica Composite Pastes with Tunable Setting Properties", Journal of Materials Chemistry B: Materials for Biology and Medicine 5, 6065–6080 (2017). [PubMed: 29104753]
87. Uskoković V, Desai TA – "Simultaneous Bactericidal and Osteogenic Effect of Nanoparticulate Calcium Phosphate Powders Loaded with Clindamycin on Osteoblasts Infected with Staphylococcus Aureus", Materials Science and Engineering C: Materials for Biological Applications 37, 210–222 (2014). [PubMed: 24582242]
88. Tseng YC, Yang A, Huang L – "How does the cell overcome LCP nanoparticle-induced calcium toxicity", Mol. Pharm. 10, 4391–5 (2013). [PubMed: 24032396]
89. Baig AA, Fox JL, Young RA, Wang Z, Hsu J, Higuchi WI, Chhettry A, Zhuang H, Otsuka M, Relationships among carbonated apatite solubility, crystallite size, and microstrain parameters", Calcif Tissue Int. 64(5):437–49 (1999). [PubMed: 10203421]
90. Dorozhkin S – "Self-setting calcium orthophosphate formulations", J Funct Biomat 4:209–311 (2013).
91. Uskoković V, Wu VM – "Calcium Phosphate as a Key Material for Socially Responsible Tissue Engineering", Materials 9, 434–460 (2016). [PubMed: 27347359]
92. Rolvien T, Barbeck M, Wenisch S, Amling M, Krause M – "Cellular mechanisms responsible for success and failure of bone substitute materials", Int. J. Mol. Sci. 19, E2893 (2018). [PubMed: 30249051]
93. Fischer CR, Mikami M, Minematsu H, Nizami S, Goo Lee H, Stamer D, Patel N, Yu Soung D, Back JH, Song L, Drissi H, Lee FY – "Calreticulin inhibits inflammation-induced osteoclastogenesis and bone resorption", J. Orthop. Res. 35, 2658–2666 (2017). [PubMed: 28460421]
94. Selvaraj V, Tomblin J, Yeager Armistead M, Murray E – "Selenium (sodium selenite) causes cytotoxicity and apoptotic mediated cell death in PLHC-1 fish cell line through DNA and mitochondrial membrane potential damage", Ecotoxicol. Environ. Saf. 87, 80–88 (2013). [PubMed: 23158585]
95. Nagy G, Benko I, Kiraly G, Voros O, Tanczos B, Sztrik A, Takacs T, Pocsi I, Prokisch J, Banfalvi G – "Cellular and nephrotoxicity of selenium species", J. Trace Elem. Med. Biol. 30, 160–170 (2015). [PubMed: 25604949]
96. Blodgett DJ, Bevill RF, Acute selenium toxicosis in sheep. Vet Hum Toxicol 1987;29:233–236. [PubMed: 3604043]
97. Mengjuan S, Zhang C, Xia IF, Cheung ST, Wong KS, Wong KH, Au DWT, Hinton DE, Kwok KWH – "Maternal dietary exposure to selenium nanoparticle led to malformation in offspring", Ecotoxicology and Environmental Safety 156, 34–40 (2018). [PubMed: 29525683]
98. Nuttall KL – "Evaluating Selenium Poisoning", Ann. Clin. Lab. Sci. 36, 409–420 (2006). [PubMed: 17127727]
99. Cummins LM, Kimura ET. Safety evaluation of selenium sulfide antidandruff shampoos. Toxicol Appl Pharmacol 1971:20:89–96. [PubMed: 5110829]
100. Quinn CF, Prins CN, Freeman JL, Gross AM, Hantzis LJ, Reynolds RJB, Yang SI, Covey PA, Banuelos GS, Pickering IJ, Fakra SC, Marcus MA, Arathi HS, Pilon-Smits EAH – "Selenium accumulation in flowers and its effects on pollination", New Phytologist 192, 727–737 (2011). [PubMed: 21793829]

101. Lee J, Sayed N, Hunter A, Au KF, Wong WH, Mocarski ES, Pera RR, Yakubov E, Cooke JP, Activation of Innate Immunity is Required for Efficient Nuclear Reprogramming", Cell 151, 547–588 (2012). [PubMed: 23101625]
102. Xia IF, Enhancing Immunity and Disease Resistance in Fish by Chitosan-Selenium Nanoparticles", Lecture at the 2018 NanoWorld Conference, San Francisco, CA (2018).
103. Espinosa A, Henriquez-Olguin C, Jaimovich E, Reactive oxygen species and calcium signals in skeletal muscle: A crosstalk involved in both normal signaling and disease", Cell Calcium 60, 172–179 (2016). [PubMed: 26965208]
104. McClung JP, Roneker CA, Mu W, Lisk DJ, Langlais P, Liu F, Lei XG – "Development of insulin resistance and obesity in mice overexpressing cellular glutathione peroxidase", Proceedings of the National Academy of Sciences USA 101, 8852–8857 (2004).
105. Hsu FT, Wei ZH, Hsuan YC, Lin W, Su YC, Liao CH, Hsieh CL – "MRI tracking of polyethylene glycol-coated superparamagnetic iron oxide-labelled placenta-derived mesenchymal stem cells toward glioblastoma stem-like cells in a mouse model", Artif. Cells Nanomed. Biotechnol. 46(sup3):S448–S459 (2018). [PubMed: 30198338]
106. Uskoković V, Desai TA – "Does Translational Symmetry Matter? Fibroblastic and Osteoblastic Interactions with the Topographically Distinct Poly(ε-Caprolactone)/Hydroxyapatite Thin Films", ACS Applied Materials and Interfaces 6 (15) 13209–13220 (2014). [PubMed: 25014232]
107. Abdo KM – "NTP Technical Report on Toxicity Studies of Sodium Selenate and Sodium Selenite Administered in Drinking Water to F344/N Rats and B6C3F1 Mice", United States Department of Health and Human Services, Research Triangle Park, NC (1994).
108. Uskoković V, Marković S, Veselinović Lj., Škapin S, Ignjatović N, Uskoković DP – "Insights into the Kinetics of Thermally Induced Crystallization of Amorphous Calcium Phosphate", Physical Chemistry Chemical Physics 20, 29221–29235 (2018). [PubMed: 30427330]

Highlights

- Selenite exerts antagonistic crystallographic effects in a concentration-dependent manner.
- Selenite preferentially replaces carbonate in the lattice of carbonated HAp, before substituting phosphate.
- Solubility of HAp increases with accommodation of selenite.
- Inhibition of RAW264.7 osteoclasts is directly proportional to the selenite content in HAp.
- The inhibitory effect is absent in osteoblastic K7M2 and MC3T3-E1 cells.

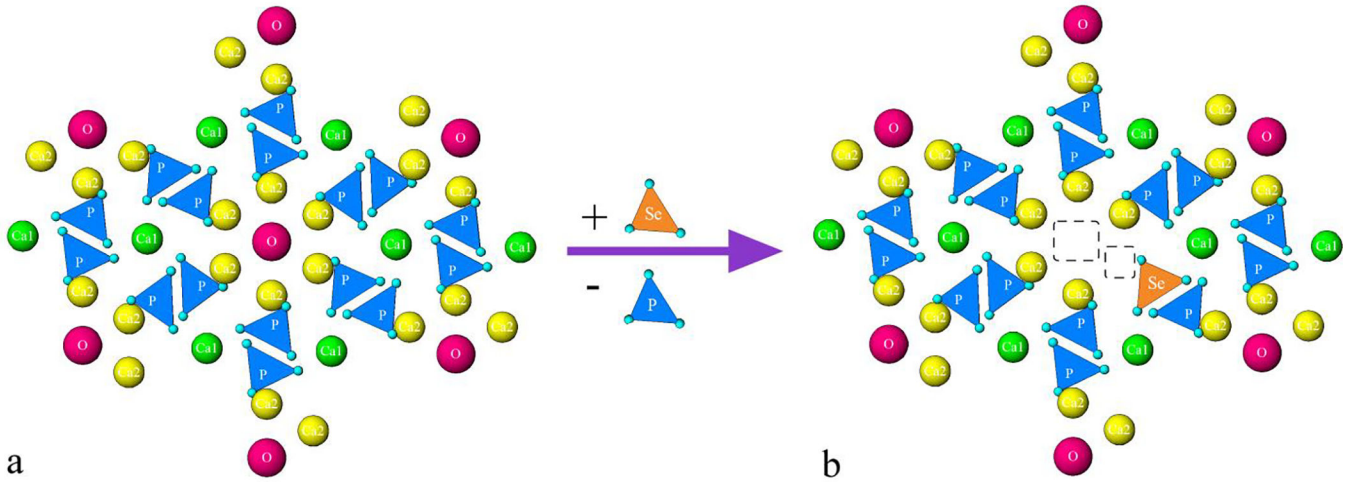

Fig.1.

Crystal structure of pure HAp viewed down the c-axis before (a) and after (b) a single phosphate-to-selenite substitution in the center, showing the two typical vacancies forming to balance the resulting cationic charge excess: Ca^{2+} and OH^{-}. Different ionic elements are represented with different colors: columnar, Ca1 calcium ions with the coordination number of 9 are green; hexagonal, Ca2 calcium ions with the coordination number of 7 are yellow; hydroxyl is magenta; phosphate is blue; selenite is orange.

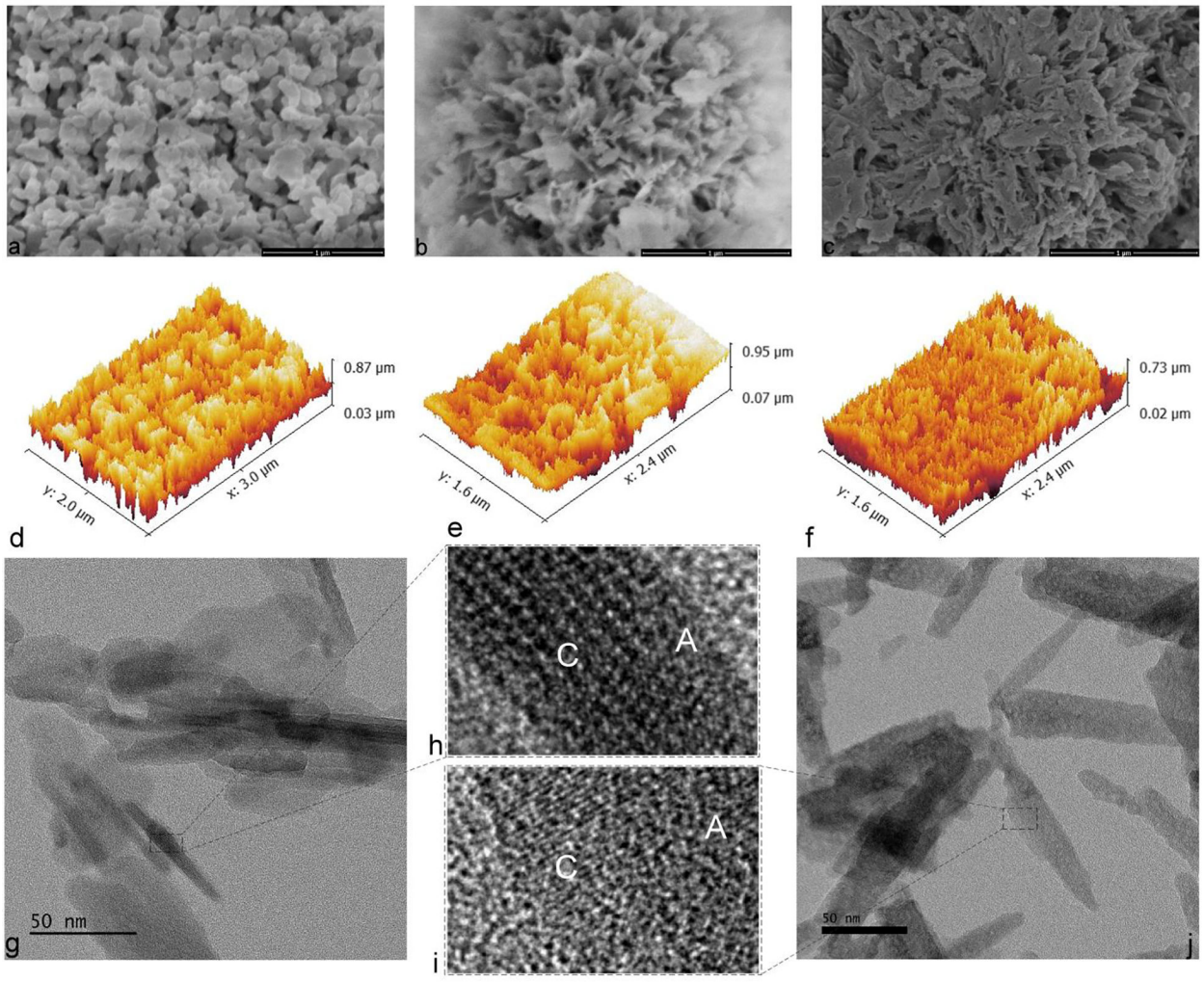

Fig.2.

Scanning (a-f) and transmission (g-j) electron micrographs of HAp powders containing 0 (a, d, g, h), 0.1 (b, e) and 1.2 (c, f, i, j) wt.% of selenite ions. Crystalline and amorphous domains in rod-shaped HAp and Se-HAp particles in (e) and (f) are denoted with C and A, respectively.

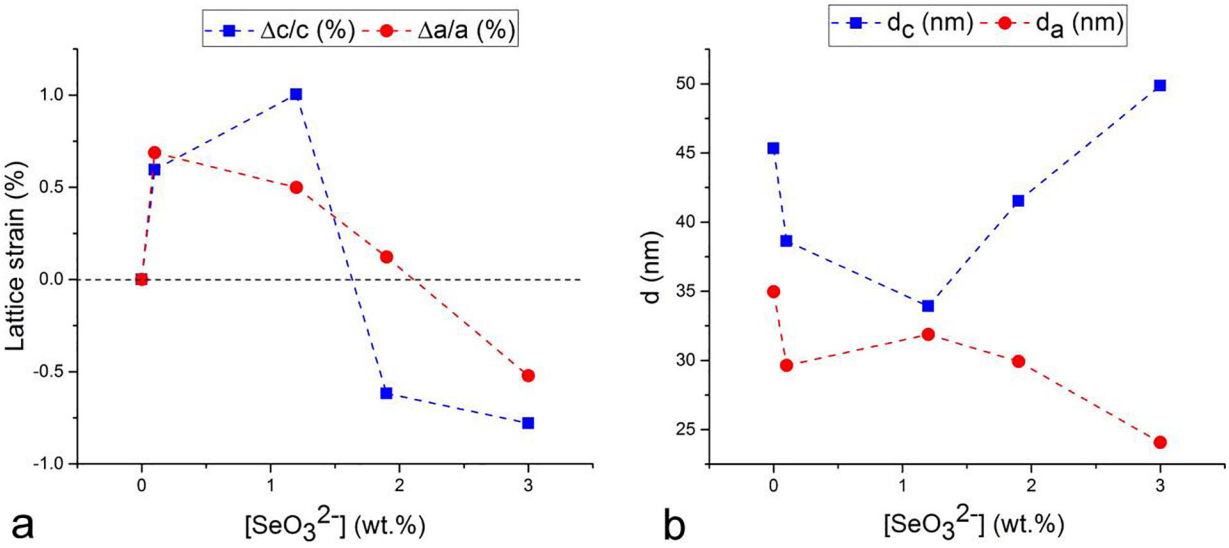

Fig.3.

Lattice strain measured as Δc/c and Δa/a in the direction of c- and a- axes, respectively, as a function of the selenite content in co-precipitated and annealed Se-HAp (a) and the average crystallite domain dimensions in the direction of c- and a- axes calculated from the broadening of the halfwidths of (002) (d = 3.440 Å, 2θ = 25.90 °) and (300) (d = 2.720 Å, 2θ = 32.90 °) diffraction peaks, respectively.

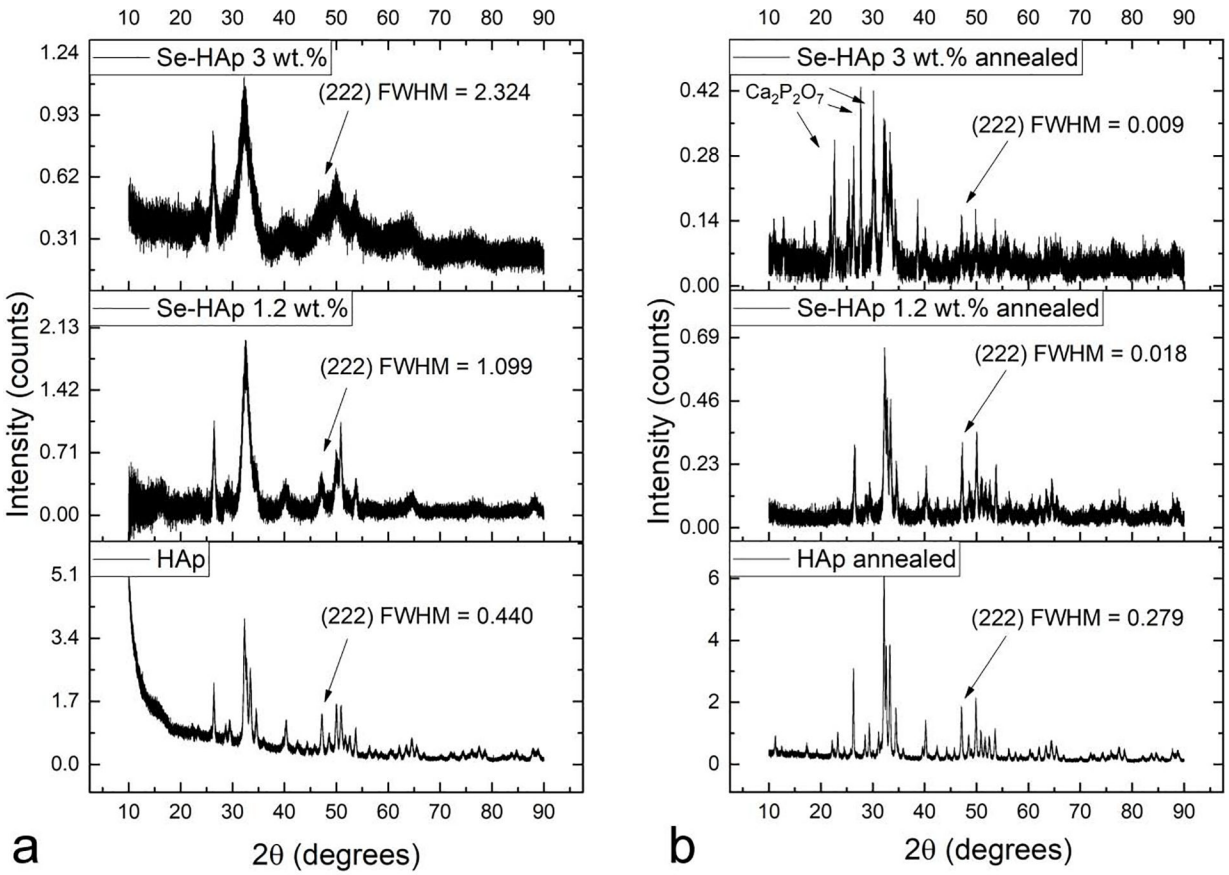

Fig.4.

X-ray diffractograms of HAp and selenite-doped HAp with two different weight contents of selenite, 1.2 and 3.0 wt.%, depending on whether the powders were as-prepared (a) or annealed (b). Full widths at half maxima (FWHM) were measured on the (222) peak at 2θ = 46.69 °, corresponding to the Bragg distance of d = 1.943 Å. $Ca_2P_2O_7$ denotes calcium pyrophosphate as the secondary phase.

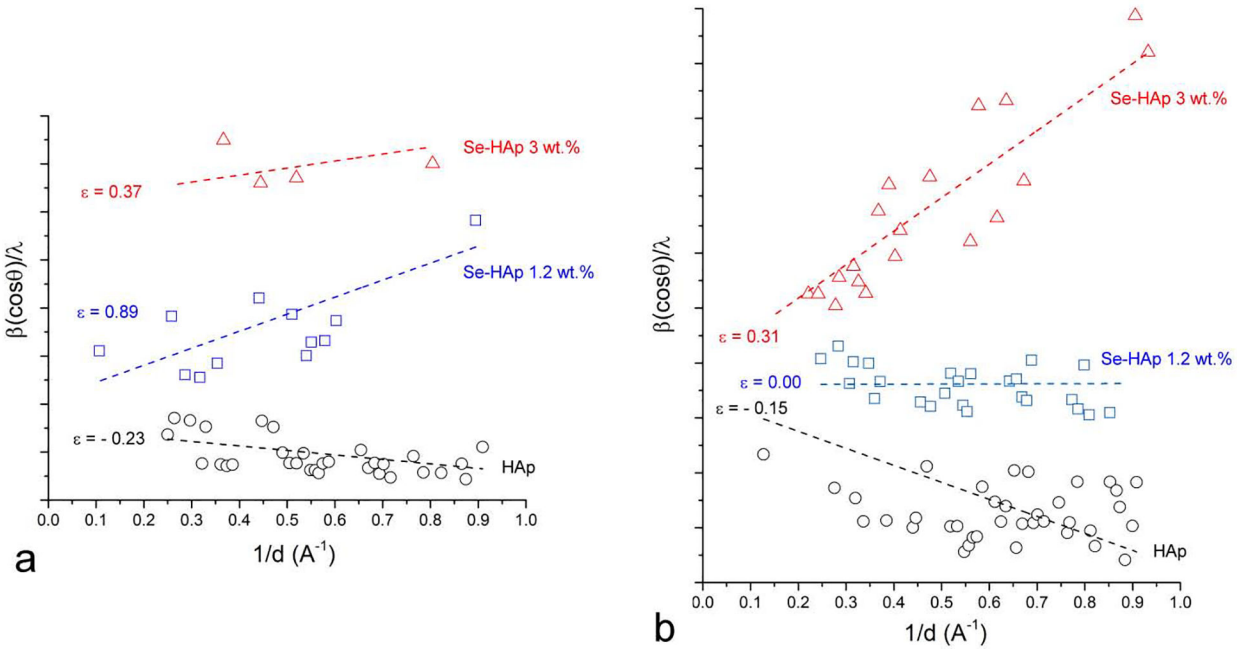

Fig.5.

Williamson-Hall plots constructed in the 0 – 1 $Å^{-1}$ range of the reciprocal lattice spacing, d for as-precipitated (a) and annealed (b) HAp powders containing different amounts of selenite: 0, 1.2 or 3.0 wt.%. ε denotes dimensionless lattice strains calculated as halved slopes of the corresponding linear fits.

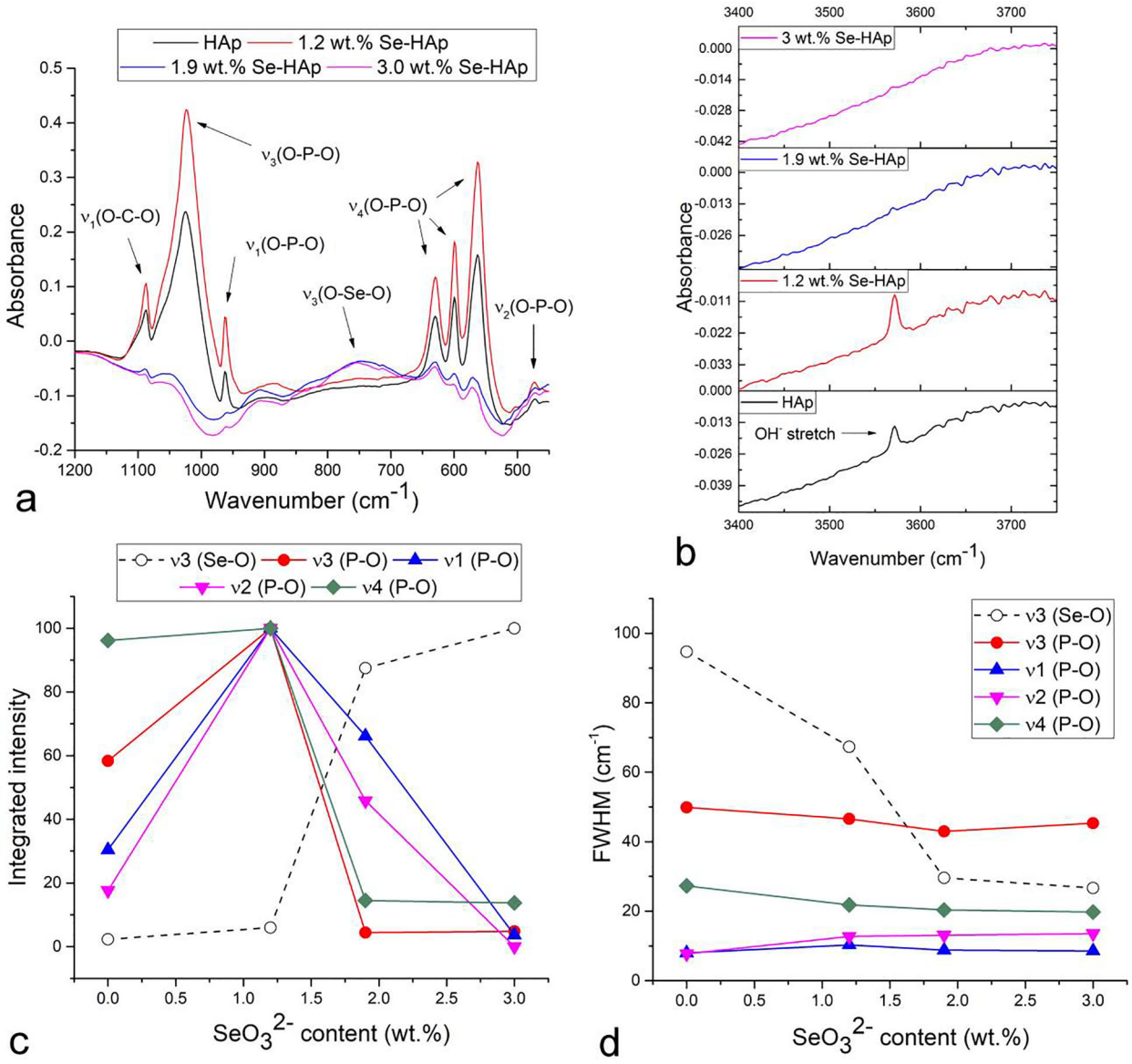

Fig.6.

FTIR spectra of HAp powders doped with different concentrations of selenite ion, ranging from 0 to 3 wt.% in the 450 – 1200 cm^{-1} (a) and 3400 – 3750 cm^{-1} (b) spectral ranges, along with the integrated intensities (c) and full widths at half maxima (FWHM) (d) of the symmetric, ν_1, and asymmetric, ν_3, stretching modes and the doubly and triply degenerated, bending modes, ν_2 and ν_4, respectively, of the phosphate tetrahedron, and the asymmetric, ν_3, stretching mode band of the selenite pyramid as a function of the selenite content in HAp.

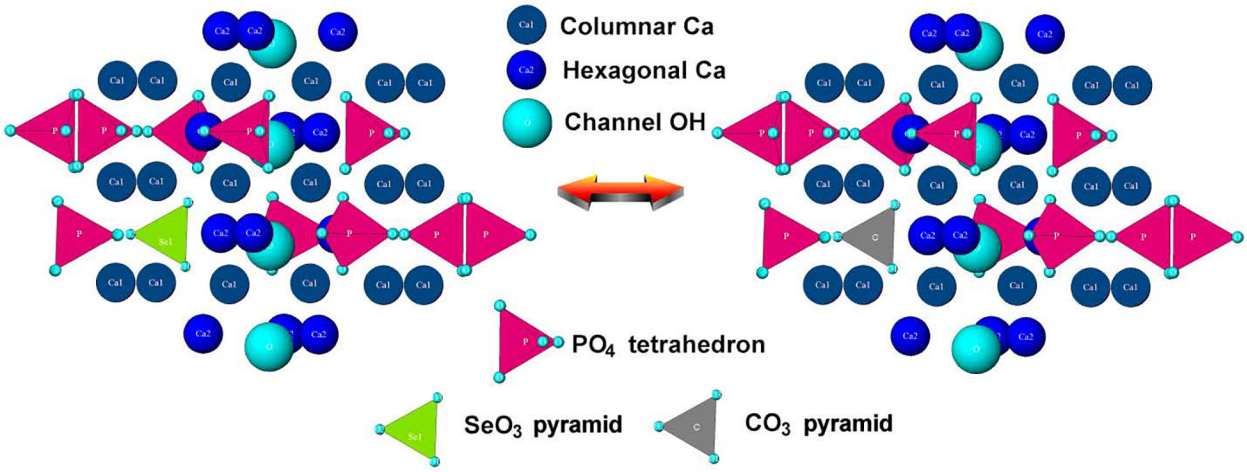

Fig.7.

Crystal structure of HAp viewed perpendicularly to the c-axis, showing the competition of selenite and carbonate pyramids for the same phosphate tetrahedron during co-precipitation of Se-HAp under ambient conditions.

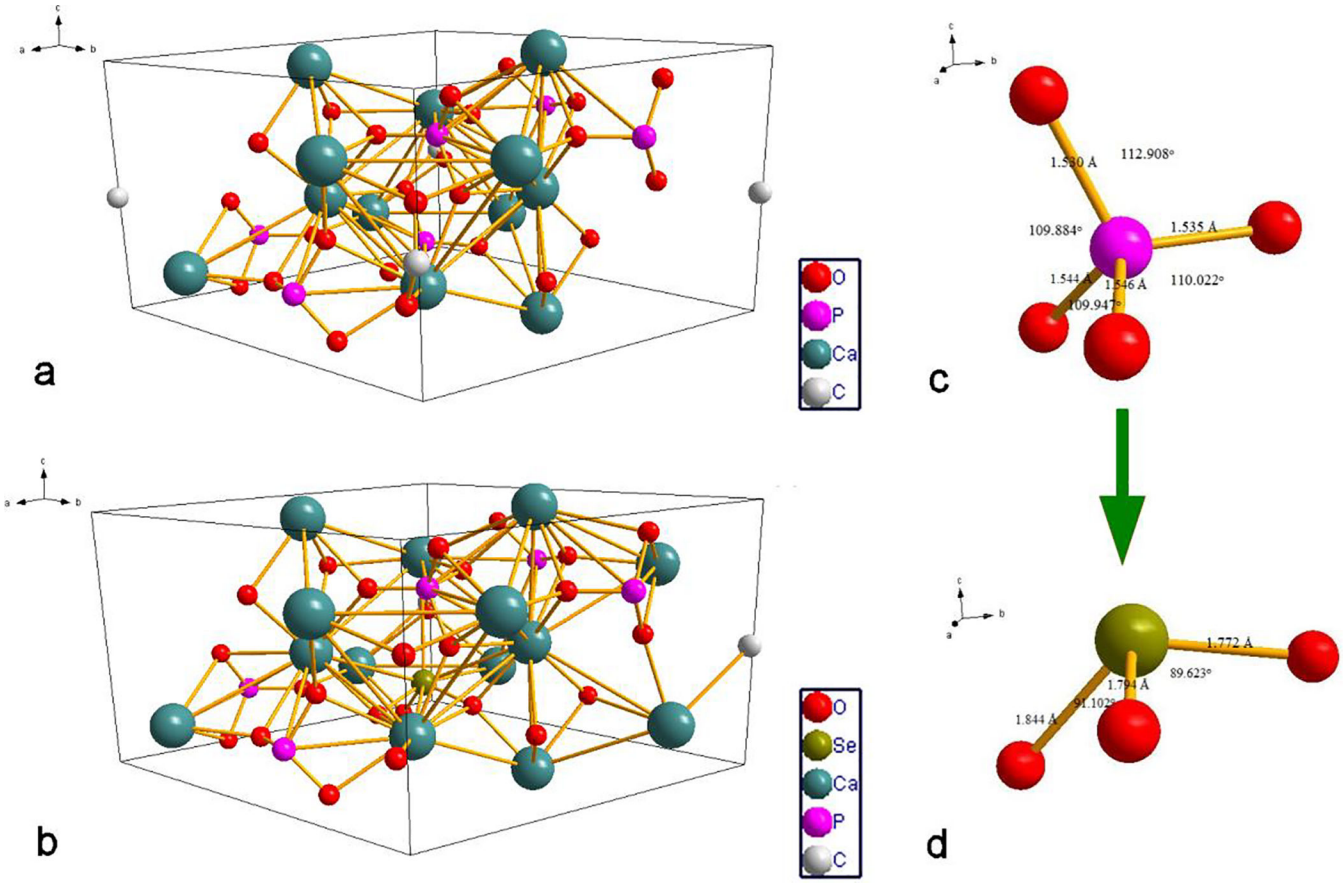

Fig.8.

The preferred geometry for A-type carbonated HAp (a) and the optimum geometry for selenite-doped A-type carbonated HAp (b). Phosphate group orientation with bond lengths and angles in A-type carbonated HAp before doping with selenite (a) and the geometry of the selenite ion in the unit cell of A-type carbonated Se-HAp (d).

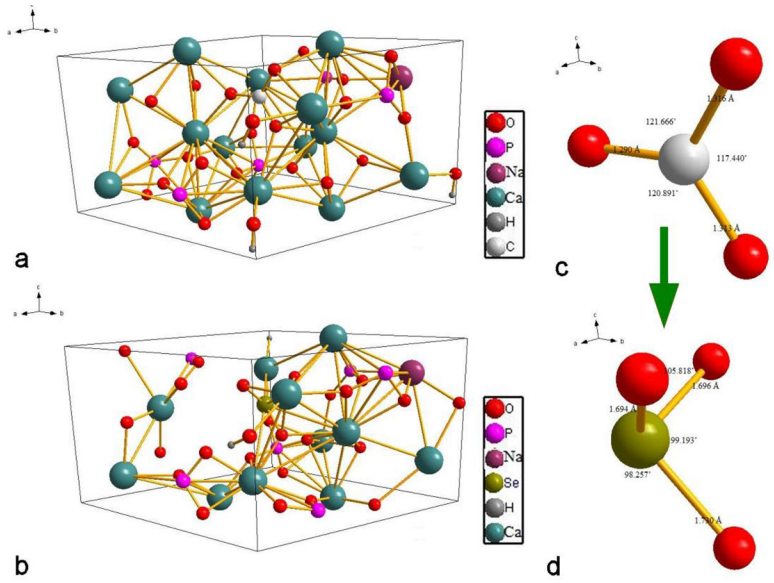

Fig.9.

The preferred geometry for B-type carbonated HAp (a) and the optimum geometry for selenite-doped B-type carbonated HAp (b). Phosphate group orientation with bond lengths and angles in B-type carbonated HAp before doping with selenite (a) and the geometry of the selenite ion in the unit cell of B-type carbonated Se-HAp (d).

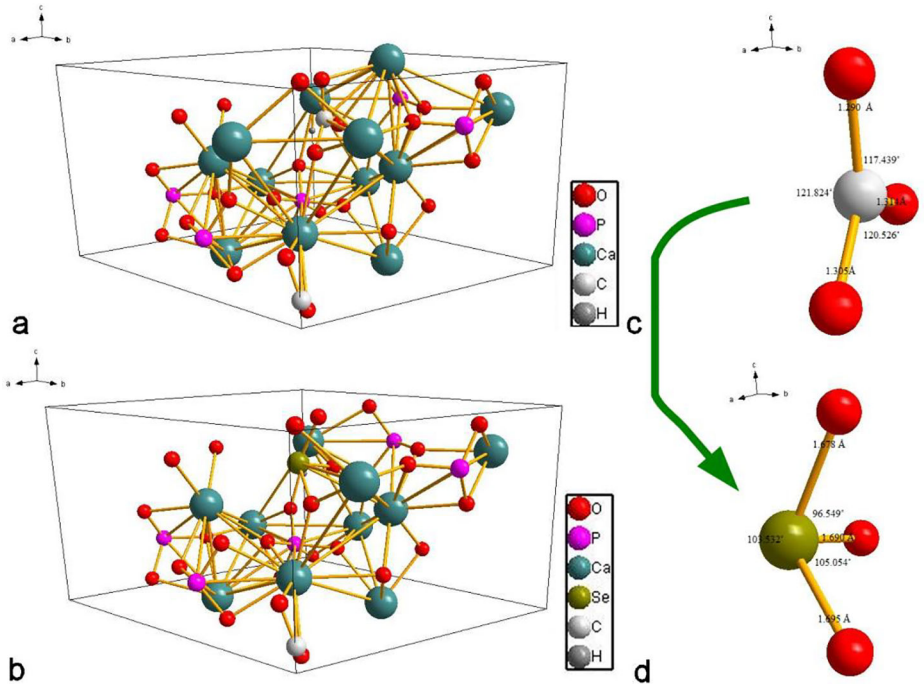

Fig.10.

The preferred geometry for AB-type carbonated HAp (a) and the optimum geometry for selenite-doped AB-type carbonated HAp (b). Phosphate group orientation with bond lengths and angles in AB-type carbonated HAp before doping with selenite (a) and the geometry of the selenite ion in the unit cell of AB-type carbonated Se-HAp (d).

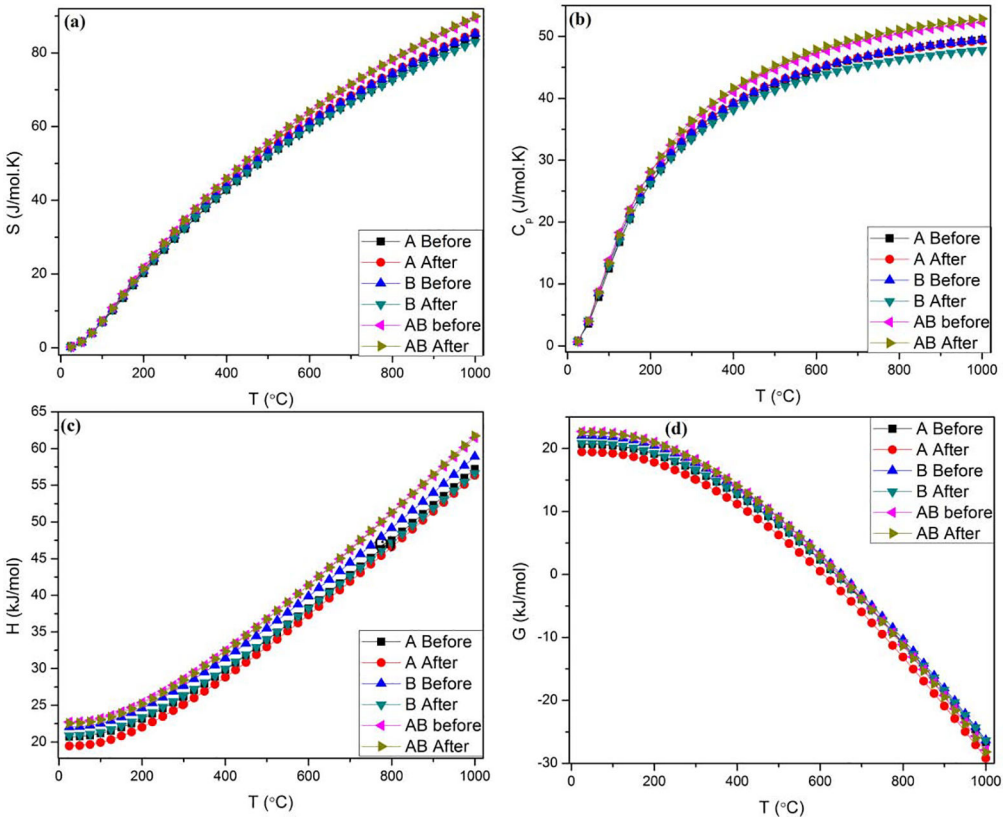

Fig.11.

Temperature profiles of selected thermodynamic parameters, including entropy (a), heat capacity (b), enthalpy (c) and the Gibbs free energy (d), depending on the type of carbonated HAp before and after the substitution with selenite.

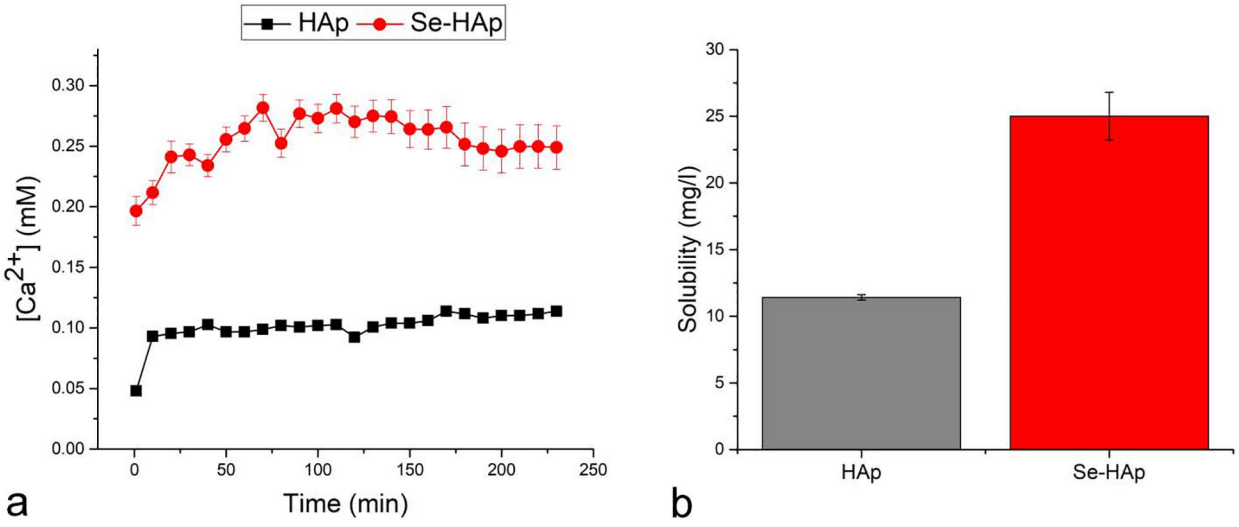

Fig.12.

Free calcium ion concentration in the aqueous supernatant in a 1 mg/ml suspension (20 mM Bis-Tris, pH 6.8, 25 °C) of as-precipitated, non-annealed HAp, either pure (HAp) or doped with 1.2 wt.% of selenite (Se-HAp) at different time points (a) and the solubility values for the two powders after 24 h of immersion time (b).

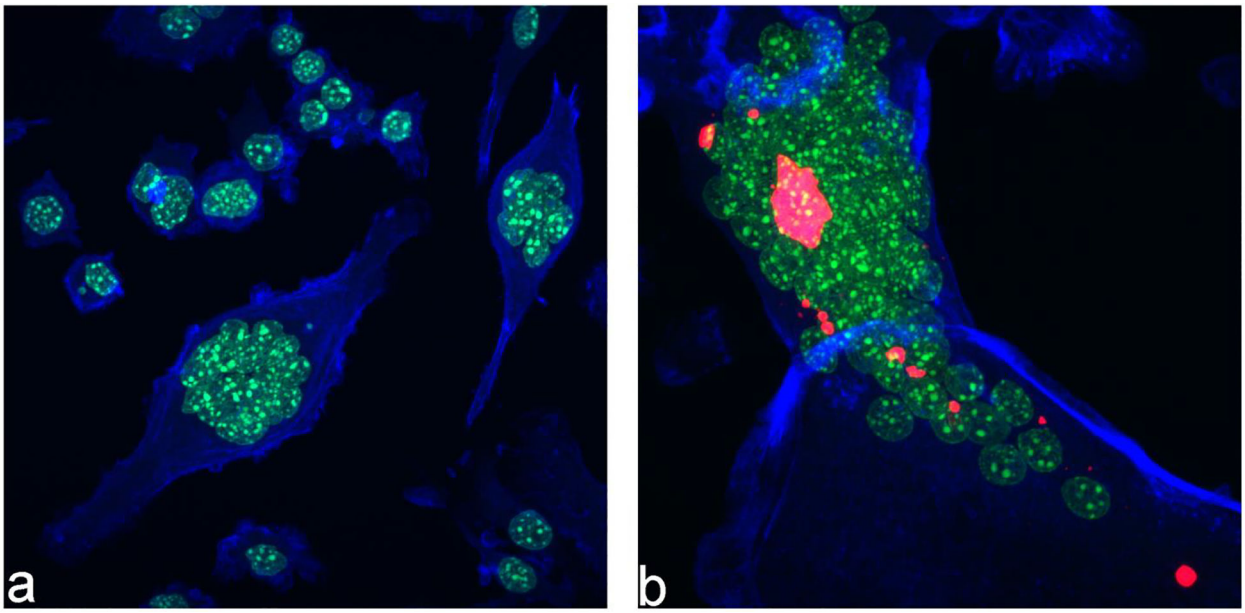

Fig.13.

Fluorescent optical micrographs of control RAW264.7 cells differentiating from mononuclear precursors to polynuclear osteoclastic cells without (a) and with (b) the presence of uptaken Se-HAp particles. Cytoskeletal f-actin microfilaments are stained in blue, cell nuclei in green and Se-HAp particles in red.

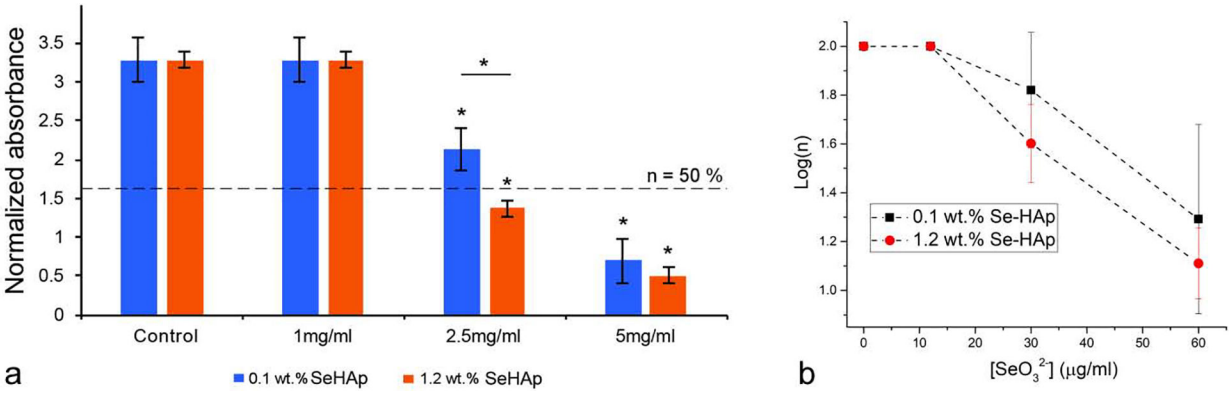

Fig.14.

(a) Absorbance at λ = 540 nm of lysed confluent RAW264.7 osteoclastic cell suspensions normalized to the absorbance of the cell culture medium, indicative of the mitochondrial dehydrogenase activity and, thus, of the cell viability, *n*, as determined by the MTT assay after 48 h of incubation with different concentrations of Se-HAp particles (1, 2.5 and 5 mg per ml of the cell culture medium) containing different amounts of the selenite ion (0.1 and 1.2 wt.%). Dashed line represents 50 % viability. (b) Logarithmic viability (log(n)) of osteoclastic RAW264.7 cells as a function of the predicted concentration of selenite ions in the medium containing partially dissolved Se-HAp particles with two different selenite contents (0.1 and 1.2 wt.%) and at three different doses (1, 2.5 and 5 mg/ml). Data points are presented as arithmetic means (n = 3) with error bars representing standard deviation. Samples with a significantly lower cell viability with respect to the control group ($p < 0.05$) are marked with *.

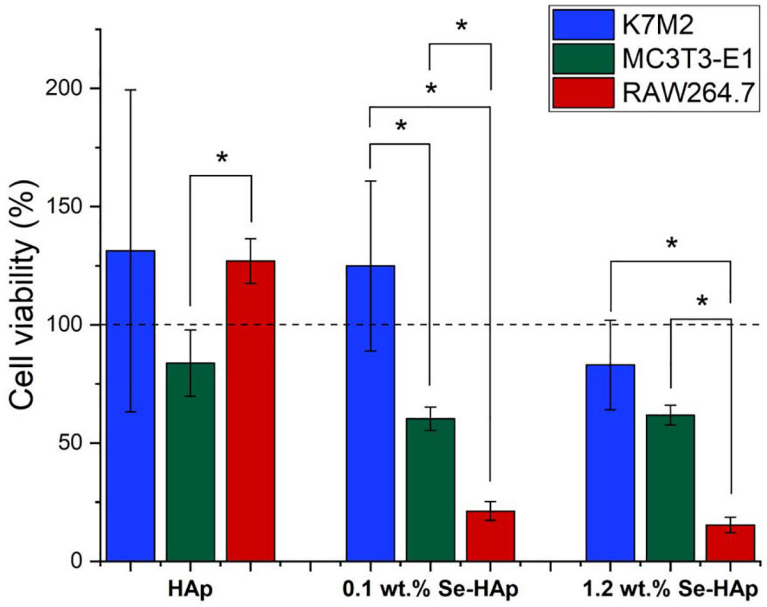

Fig.15.

Comparative cell viabilities of K7M2 and MC3T3-E1 osteoblastic cells and RAW264.7 osteoclastic cells, as determined by the MTT assay after 48 h of incubation with 5 mg/ml HAp or Se-HAp particles containing different amounts of the selenite ion (0.1 and 1.2 wt.%). Dashed line represents the 100 % viability of the negative control cells not challenged with any particles. Data points are presented as arithmetic means (n = 3) with error bars representing standard deviation. Samples with a significantly lower cell viability with respect to the control group ($p < 0.05$) are marked with *.

Table 1.

Concentrations of selenite, calcium and phosphate ions in the reaction solutions at the onset of precipitation and the weight percentage of selenite ions in the solid product, as determined by ICP-MS, along with the theoretical Ca/P and P/Se ion ratios in the final solid product.

$[SeO_3^{2-}]$in (V = 200 ml) (mM)	$[Ca^{2+}]$in (V = 200 ml) (mM)	$[PO_4^{3-}]$in (V = 200 ml) (mM)	$[SeO_3^{2-}]$final (wt.%)	[Ca/P] molar ratio	[P/Se] molar ratio
0.69	44.00	28.20	0.1	1.67	0.8
1.38	44.00	28.20	1.2	1.69	9.2
2.07	44.00	28.20	1.9	1.71	14.6
2.76	44.00	28.20	3.0	1.74	23.0

Table 2.

Dependence of the surface topography parameters, including average roughness (R_a), root mean square roughness (R_q), maximum height of the roughness (R_t) and maximum roughness valley depth (R_v) on the selenite dopant content in Se-HAp.

Sample	R_a (nm)	R_q (nm)	R_t (nm)	R_v (nm)
HAp	25.3	32.1	245.7	133.8
0.1 wt.% Se-HAp	28.9	36.3	257.8	123.8
1.2 wt.% Se-HAp	31.3	39.4	253.0	125.2

Table 3.

Activation energies for the crystallization of amorphous domains in HAp and Se-HAp precipitates with different selenite contents upon annealing to 800 °C.

Sample	E_a (kJ/mol)
HAp	22.4
0.1 wt.% Se-HAp	33.1
1.2 wt.% Se-HAp	67.6
3.0 wt.% Se-HAp	121.4

Table 4.

Variation of the unit cell parameters a, b and c in (Å), the angles α, β and γ in (°), and the unit cell volume Q in ($Å^3$) before and after the SeO_3^{2-} substitution in different forms of carbonated HAp.

	a (Å)		b (Å)		c (Å)		α (°)		β (°)		γ (°)		Ω ($Å^3$)	
	Before	After	Before	After	Before	After	Before	After	Before	After	Before	After	Before	After
A-cHAp	9.567	9.441	9.910	9.522	6.816	6.880	89.888	89.734	90.750	90.308	117.995	119.604	570.574	537.744
B-cHAp	9.441	9.739	9.522	9.732	6.880	6.951	89.734	94.369	90.308	85.028	119.604	121.655	537.744	558.318
AB-CHAp	9.481	9.437	9.900	9.797	6.870	6.755	90.093	90.218	89.111	89.319	118.014	118.287	569.153	549.959